NextGEM

Next Generation Integrated Sensing and Analytical System for Monitoring and Assessing Radiofrequency Electromagnetic Field Exposure and Health

D3.7: Development of innovative self-monitoring tools and methodologies - Final version

Document Summary Information

Start Date	1/07/2022	**Duration**	48 months
Project URL	https://www.nextgem.eu/		
Deliverable	D3.7: Development of innovative self-monitoring tools and methodologies - Final version		
Work Package	WP3	**Task**	T3.3
Contractual due date	31/10/2024	**Actual submission date**	31/10/2024
Type	Report	**Dissemination Level**	PU-Public
Lead Beneficiary	TUD	**Deliverable Editor**	Marco Spirito (TUD)

This project has received funding from the European Union's Horizon Europe research and innovation programme under the Grant Agreement No 101057527

Contributors and Peer Reviewers

Contributors
Marco Spirito, Leila Gottmer (TUD), Erdal Korkmaz, Fidelis Theinert, Sam Aerts, John Bolte, Jonathan Gnanadha, Derek Land (THUAS), Fulvio Schettino, Marco Donald Migliore (UCAS), Olga Zeni (CNR), Nikolaos Petroulakis (FORTH), Eduardo Soudah (CIMNE), Loek Colussi (AT), Yuri Feldman (HUJI)
Peer Reviewers
Stefanos Fafalios (SANL), Loek Colussi (AT), Erdal Korkmaz (THUAS)

Revision history (including peer-reviewing and quality control)

Version	Issue Date	Changes	Contributor(s)
v0.1	01/06/2024	Table of Contents provided	Marco Spirito (TUD)
v0.2	30/06/2024	Sections populated with the Task leaders	Marco Spirito (TUD), Erdal Korkmaz (THUAS)
v0.3	15/07/2024	Section defined assigned, and agreed	All partners
v0.4	31/07/2024	First contributions	All partners
v0.5	15/08/2024	Integration and harmonization	Marco Spirito (TUD), Erdal Korkmaz (THUAS)
v0.6	31/08/2024	Second contributions	All involved partners
v0.7	20/10/2024	Complete version ready for peer review	Marco Spirito (TUD)
v0.8	23/10/2024	Peer review	Erdal Korkmaz (THUAS), Marco Spirito (TUD)
v0.9	28/10/2024	Comments addressed from peer review, technical and quality assurance	Mats-Olof Mattsson (SPi), Nicolas Louca (EBOS), Marco Spirito (TUD)
v1.0	31/10/2024	Final review and submission	Nikolaos Petroulakis (FORTH)

Disclaimer

Copyright message

Table of Contents

List of Figures

List of Tables

Glossary of terms and abbreviations

Abbreviation / Term	Description
ADC	Analog-to-Digital Converter
AUT	Antenna under Test
CAD	Computer-Aided Design
CSV	Comma-separated values
DC	Direct Current
DR	Dynamic Range
EMF	Electro Magnetic Fields
FD	Frequency Domain
FR1/FR2	Frequency Range (FR1 5G NR <7.125 GHz, FR2 5G NR >24.250 GH)
FS	Full-Scale
GPS	Global positioning system
HW	Hardware
LNA	Low Noise Amplifier
MaMIMO	Massive Multiple Input Multiple Output
MCU	Micro-controller unit
MPE	Maximum Power Extrapolation
PBCH	Physical Broadcast Channel
PCB	Printed circuit board
RISC	Reduced Instruction Set Computing
RMS	root-mean-square
RTC	Real time clock
RTSA	Real time Spectrum Analyzer
SDR	Software Defined Radio
SNR	Signal to Noise Ratio
SPI	Serial Peripheral Interface
SSB	Synchronization Signal Block
USB	Universal serial bus
VGA	Variable Gain Amplifier
VNA	Vector Network Analyzer

Executive Summary

In Deliverable D3.3, we provided an in-depth overview of the architecture choices and design process, including the modelling of various subsystems. We also identified the characterization and calibration procedures to be employed for developing innovative self-monitoring tools for RF-EMF exposure.

The deliverable initially summarized the activities conducted in Task 3.1, which aimed to present the state of the art in low-power sensing units and define the requirements for innovative units targeting the FR2 band. These sensing units are designed to continuously measure the channel power radiated at the chosen application frequency in real-world environments. Additionally, the deliverable summarized the work of Task 3.3, which focused on defining the engineering processes required to translate these requirements into modelling and design procedures. This effort will ultimately lead to the hardware development of both the passive and active subsystems of the FR2 sensing nodes.

The resulting hardware – designed, fabricated, and characterized – will be used by the consortium to conduct EMF measurement campaigns, specifically the NextGEM case studies outlined in WP7.

In this deliverable, we extend the design and characterization analysis by describing specific steps in the fabrication process of a low-cost, high-sensitivity sensor for the FR2 band. First, we present the 3D printing approach used to create lenses that focus radiated/received energy. Next, we provide a detailed description of the final selected layer stack in the board prototype, which allows the co-integration of the high-performance radiating interface and high-sensitivity, high-resolution RF electronic circuitry. We also discuss the real-time processing of data continuously generated by the sensor and the extraction of key statistical metrics, which are stored in non-volatile memory. Finally, we present the measurement results of the first prototype of the radiating front-end.

Further details are provided regarding the emulative environments in which the sensors will be placed and the analyses that will be conducted to assess the measurement results during the case studies of WP7.

1 Introduction

Commercial (high-end) instrumentations capable of performing standardized measurement protocols are offered by all the main vendors and used by government agencies to check compliance with respect to basic restrictions. On the other hand, sensing nodes capable of acquiring the RF-EM for realistic exposure levels [1][2]and carrying out non-standardized measurement protocols (in the FR2 bands) are currently missing. Among the reasons for this offering gap, two main contributors can be highlighted:

i) The higher carrier frequency (i.e., above 24.5GHz) and the larger modulation bandwidth (i.e., up to 400MHz) when compared with FR1 system, makes the usage of low-cost high-sensitivity sensing nodes, like the SDR-based sensor nodes described in D3.1 [2][3], not feasible given their frequency limitation to below 6GHz. This imposes a need to redefine the architecture topologies to be employed at these frequencies and carefully analyse the requirements of the various building blocks. These considerations are detailed in Section 2 of this deliverable.

ii) The increased losses present at the higher frequencies, and the (increased) noise of each component of the sensing nodes, from the receiving antenna to the digitizer unit. These increased systems losses are also set by the (higher) conductive and dielectric losses of the interconnecting elements realized in the PCB platform.

Optimizing such systems requires a strong multidisciplinary knowledge together with a complex design and modelling flow integrating full wave simulation with active device response, reducing the number of groups in the scientific community able to carry out such a complex task. The design, simulation and validation methodologies employed in Task 3.3 by the members of the consortium are described in Section 3.

The work reported here, which was carried out in Task 3.3, has been realized in strong co-operation with the team in charge of case study 3 of WP7. This allows the sensor node designed and characterized in this task to be a "direct fit" to the monitoring vest, which will realize the self-monitoring tool to be used in case study 3. Both the interfaces from the data acquisition standpoint, as well as the communication between the subsystems, have been taken into account in the design and development of the sensing node. In addition, the generation of 5G-compliant signals using low-cost equipment, developed in Task 3.3 to support the characterization of the sensing node, has also been transferred to support part of the activities to be carried out in Task 4.2.

1.1 Mapping NextGEM Outputs

The purpose of this section is to map NextGEM's Grant Agreement (GA) commitments, within the formal task description and deliverables, against the project's respective outputs and work performed.

Table 1: Adherence to NextGEM's GA Tasks and Deliverables Descriptions.

TASKS	
Task Number & Title	**Respective extract from formal Task Description**
Task 3.3 – Development of innovative self-monitoring tools and methodologies	The goal of this task is to develop innovative low power sensing units, capable of acquiring continuously the channel power received by the node under a given solid angle (i.e., set by the lens design) and store it in a non-volatile memory for further acquisition and processing. The sensing node will be based on dual polarized antennas, employing plastic lenses to increase the received power, i.e., relying higher gain antennas. The required amplification level and the noise figure trade-offs will be analysed in the context of sensor node capable of detecting EMF level readout in realistic application scenarios. The node will be further tested using lab equipment, under signal and multi-source excitation employing standards compliant with 5GNR operating in the FR2 frequency band. After the completion of the sensor node characterization, the design will be employed in collaboration with the project partners to be integrated in the sensing vest realizing the self-monitoring tool to be used in case study 3.
DELIVERABLES	
Deliverable D3.7: Development of innovative self-monitoring tools and methodologies - Final version (M28)	

This deliverable will give a description of the design, development and implementation of wearable 5G sensors.

1.2 Deliverable overview and report structure

Based on the work conducted under Task 3.3 and its set objectives, this document begins with an Executive Summary, followed by the introduction in Section 1.

Section 2 discusses the key performance metrics of the sub-blocks that compose the wearable sensor, along with the trade-offs at the architectural level.

In Section 3, the simulation, modelling, and measurements of the proposed FR2 sensor are described in detail.

Section 4 explores the two use cases—static deployable and wearable nodes—from a system-level perspective. It also addresses the number and relative locations of the sensors, using the received field compared to an isotropic antenna as the key metric.

Section 5 focuses on the installation of the FR1 nodes in the Green Village and discusses the concept of the static deployable node and wearable vest for FR2 field measurement campaigns in emulative environments.

Finally, Section 6 presents the conclusions of the deliverable.

1.3 Updates from previous Deliverable D3.3 "Development of innovative self-monitoring tools and methodologies"

Deliverable 3.7 includes several amendments and extensions compared to the initial version, D3.3. These updates include:

- Revised Section 3.2: "Lens Antenna Design and Simulation" has been expanded to include simulations with the final PCB layer stack and the optimized antenna dimensions.
- New Section 3.2.1: "3D Printed Antenna Prototypes" describes the characterization of the printing material and the procedures for creating the antenna prototypes.
- New Section 3.2.2: "Final Board Environment Including Lens and Electronics" introduces the final layout of the PCB-integrated FR2 sensor.
- New Section 3.3.1: "Microcontroller Logger Data Flow" details the two-level hierarchy of the logging system.
- Updated Section 3.4: "OTA Testing of the First Prototype" presents and discusses the measurements of the lens antenna prototype.
- New Section 3.4.4: "5G Compliant Signal Generation and Up-Conversion" describes the signal generation and up-conversion process to create a 5G NR emulative environment.
- Updated Section 5.1: "Static Sensor Deployment at the Green Village" now includes the radiation characteristics of the base station intended for FR2.
- New Section 5.2: "Static Sensor Deployment Indoors at TU Delft" describes the antenna characteristics for the indoor emulative environment.

2 Frequency-selective architectures

In the previous work in NextGEM (D3.5: EMF sensing technologies and measuring equipment - Final version), the deliverable provided a comprehensive review of the EMF sensing technologies and the measuring equipment that are present in the current commercial and research landscape. The deliverable also highlighted the scarce availability of portable, low-cost, and low-power sensing nodes operating in the FR2 band. More specifically, D3.5 detailed the various topologies of instruments capable of identifying the time-varying field intensity in a frequency/code-selective fashion. These instruments (high-end commercial test benches) can provide an estimation of the maximum-field level based on the SSB/PBCH using a spectrogram functionality (Figure 1 a) [4] or can enable a code selective measurement when a full bandwidth demodulation is present, i.e., RTSA, (Figure 1 b).

a)  b) 

Figure 1: High-end Spectrum Analyzer and Real time Spectrum Analyzer from commercial vendors: a) Rohde & Schwarz, b) Keysight Technologies.

In both topologies, these instruments are high-end table-top equipment which requires "net-like" power sources and cannot be envisioned for real-life scenarios measurement campaigns [5] (i.e., carried out with volunteers to collect network activity and exposure levels).

For the applications envisioned in case study 3 (WP 7), an architecture based on a narrow band (i.e., 24.5-27.5 GHz) power detector is selected. These systems can be realized in a very compact fashion with low-power requirements (i.e., battery-operated). A root-mean-square (RMS) power detector can provide the cumulative time-averaged field value over the frequency band the unit is designed for (often limited by the antenna bandwidth or an optional filter).

The sub-systems composing these meters are shown in the simplified scheme block of Figure 2, where the reader can identify the antenna, the variable gain amplifier (VGA, often realized by LNA followed by a variable gain block), the power detector, providing at the output a constant (DC) voltage proportional to the RF power at its input and as last block the analog to digital converter (ADC) providing at its output a digital quantized value of its input voltage.

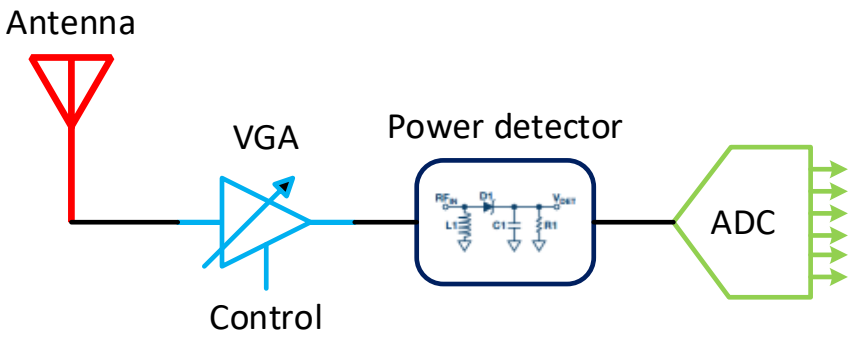

Figure 2: Simplified block scheme of a sensing node based on a power detector, including the antenna interface, the variable gain amplifier, the RMS detector, and the converter to provide a digital output.

The systems sketched in Figure 2 do not provide frequency or code-selective information; for this reason, they cannot be used to estimate maximum field levels. Nevertheless, they can be designed with sufficient bandwidth to cover the entire application band (i.e., European FR2) and sensitive enough to provide information such as the

base stations downloads duty cycles (i.e., intervals when the base station are transmitting or receiving) which is a key information to validate/refine statistical approximations employed in maximum power extrapolation (MPE) methods.

To reach the above-mentioned required performance levels, these systems need to be designed to optimize the various trade-offs at the sub-system level between sensitivity and power consumption. Only doing so can enable continuous operation with a fine temporal resolution (i.e., below a single frame duration) for a sufficiently long time-span (i.e., several hours). The figures of merits and the requirements of each of the building blocks of Figure 2 are described in detail in the next sections.

2.1 Antenna interface, figures of merit and requirements

The antenna is the sub-system that allows the conversion of the fields processed by a circuit and transported with guided structures (i.e., transmission lines) into propagating electromagnetic waves and, by reciprocity, collects power from incoming electromagnetic waves and transforms them into the source for the circuit blocks.

Antennas radiate spherical waves that propagate in the radial direction for a coordinate system centered on the antenna. At large distances, spherical waves can be approximated by plane waves.

Far from the antenna, we only consider the radiated fields and power density. The power density of the electromagnetic wave is expressed by the Poynting vector, denoted with S.

Since in a radiated wave S is proportional to $1/R^2$ (where R^2 represents the steradian, the unit of solid angle) it is convenient to define radiation intensity in order to remove the $1/R^2$ dependence as shown in Equation 2.1.

$$U(\theta,\varphi) = S(R,\theta,\varphi)R^2[W/solid\ angle] \tag{2.1}$$

A key performance parameter of antennas is the gain, which represents the ability of the antenna to direct the input power into radiation in a particular direction. This can be simply visualized as an increase of the radiation intensity in the direction of the peak radiation, as shown in Equation 2.2.

$$U = U_0 G \tag{2.2}$$

Where U_0 represents the radiation intensity of an isotropic antenna, i.e., an antenna which radiates uniformly in all directions in three-dimensional space.

The gain in a passive component, as is an antenna, is then achieved by directing the radiation away from other parts of the radiation sphere. This latter concept is important to identify the design parameter Gain as a trade-off element which can, from one side be used to increase the energy received by the detector, but on the other side implies a reduction of the portion of the sphere that can be observed by one sensing node.

Two other key parameters have a direct impact on the radiated/received power by the antenna, i.e., material losses and reflected power due to poor impedance match. The first can be minimized by choosing materials which exhibit good RF performance. The latter can be avoided with a properly addressed design process where the electromagnetic solvers and the properties of the materials employed in the fabrication of the antenna are well known.

2.2 LNA/VGA and detector, figures or merit and requirements

Given the proportionality of the power density to $1/R^2$, we can plot the expected power at the antenna interface as a function of distance from the source, for a frequency of 26.5GHz and assuming an effective isotropic radiated power of 40dBm, shown in Figure 3.

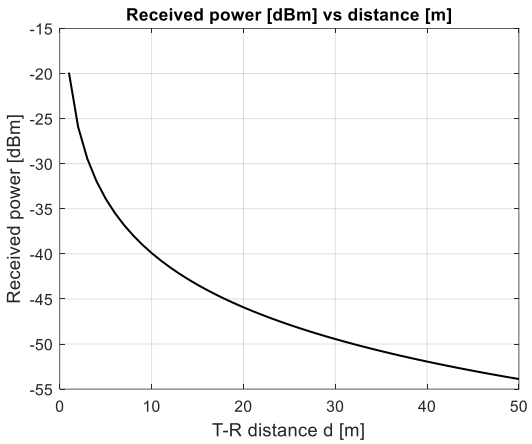

Figure 3: Results of the Friis transmission equation assuming a frequency of 26.5GHz and a power at the transmitter of 40dBm.

From Figure 3, we can derive that, in realistic case scenarios, as the ones that will be considered in Task 7.3, where the measurements will be conducted at various distances from the base station unit, the expected power variation at the sensor will be in the order of 40dB, for a distance range of ~50 meters.

Considering that commercially available RMS detectors, operating in the FR2 band, provide a maximum measurement dynamic range (i.e., range of detectable power level from the noise level to the compression level) of less than 40dB [6], it becomes clear that a varying amplification level to dynamically shift the measurement dynamic range (DR) to the right level is necessary. This function is implemented, in an electronic circuit, by a low noise amplifier (LNA), which is the first active stage of the sensor, as shown in Figure 2, with a varying gain or attenuation level capability.

The usage of the low noise amplifier (noise figures in the FR2 band for commercially available amplifiers are in the order of 2dB) as the first element of the receiving chain, allows to set the overall noise of the system to the value of the LNA. This can be simply shown by analysing Equation 2.3, and assuming a gain of the amplifier (G_1) above 20dB (i.e., 100 in linear), shown in Figure 4 (where a two-stage case is considered).

$$F_{total} = F_1 + \frac{F_2 - 1}{G_1} + \frac{F_3 - 1}{G_1 G_2} + .. + \frac{F_n - 1}{G_1 G_2 \ldots G_{n-1}}$$

(2.3)

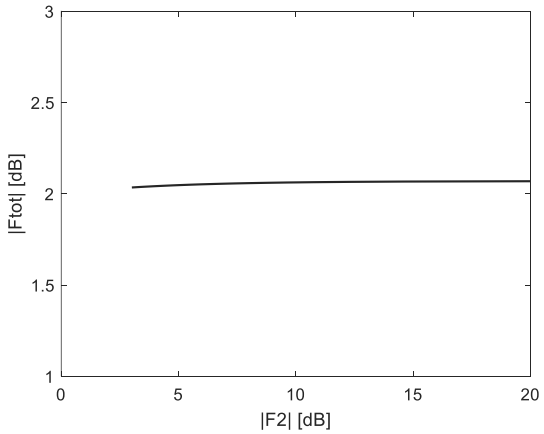

Figure 4: Result of the Friis formulas for noise for a two-stage circuit where is assumed the first stage to be an LNA with F_1 equal to 2dB and a gain equal to 20dB versus the noise figure of the following stage.

The variable gain functionality can then be implemented by adding a tuneable element (i.e., attenuator) after the LNA. Placing the attenuator after the LNA is a logical choice given Equation 2.3, since the opposite configuration (i.e., attenuator first) would provide the same level of signal but a noise figure which is the one of the attenuators (often assumed to be the same value as the attenuation) plus the one of the LNA divided by the "gain" (value lower than 1) of the attenuator, which results in a noise figure amplification.

Finally, the last block of the RF front end is composed of an RMS power detector. This component provides at its output a DC voltage which is an accurate representation (proportional) of the average signal power applied to the RF input. An example of the response of an RMS power detector measured at 26.5GHz is shown in Figure 5.

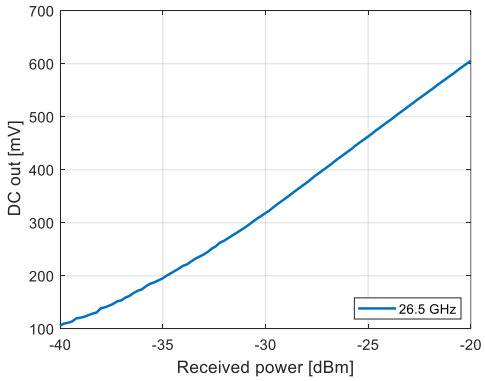

Figure 5: Measured DC output of an RMS power detector operating at 26.5GHz.

2.3 Digitizer (ADC), figures or merit and requirements

Analog to digital converters are components (i.e., integrated circuits) that convert an analogue signal into a digital word with a resolution set by the quantization level of the least significant bit (LSB), see Equation 2.4. The voltage value of the LSB is given by the number of bits (i.e., vertical scale of the ADC) and the full-scale analogue level (Vref).

$$LSB = \frac{V_{ref}}{2^N} \tag{2.4}$$

where N is the number of bits.

The transfer function between the analogue input voltage and the digital code is sketched in Figure 6.

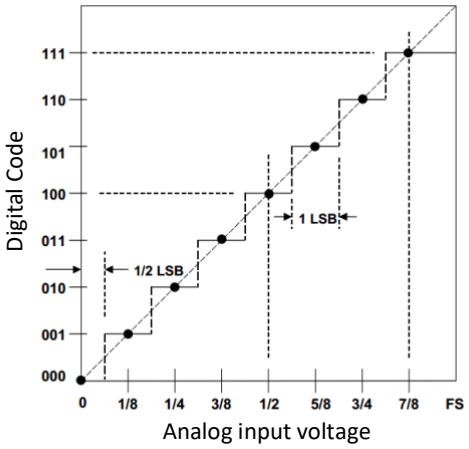

Figure 6: Digital code versus the analogue input voltage expressed as a ratio of the full scale (FS) for a 3 bit ADC.

If a full-scale (FS) sine wave is applied to the input of the ADC, the maximum theoretical signal to noise ratio (SNR) is determined by Equation 2.5.

$$SNR = 6.02N + 1.76\ [dB] \tag{2.5}$$

For the case of a 12-bit ADC, Equation 2.5 provides an SNR of 74dB.

For the FR2 band-specific detector application, the ADC should be selected with an LSB value below the output integrated noise of the detector front-end. This corresponds to the noise level at the (analogue) output of the RMS detector when no power is applied at the antenna input.

In addition to the number of bits that an ADC uses to represent the analogue signal, another important parameter is the number of samples that the ADC can acquire per second, which is defined as the sample rate (expressed in samples per second).

When considering the application of FR2 power detectors, it is important to recall that the duration of a slot in a 5G NR system can vary between 62.5 μsec to 1 msec. Given that the slot is the smallest structure of a 5G frame, in order to properly capture the power in each slot, a sampling frequency for the ADC that is faster than an 8 K sample per sec is required.

2.4 Microcontroller, figures or merit and requirements

The last component of the system, after the data has been converted into bits, is the microcontroller. The microcontroller is a compact integrated circuit embedded in the sensor to control and interface the sensing node in the larger architecture of the wearable device where it will be incorporated. The microcontroller has the function to store the data that it is (continuously) reading from the ADC into a memory. Here, the processing unit of the microcontroller can perform a set of instructions (i.e., average, time stamp, and basic/simple statistics) for the incoming data. It then uses its input/output peripherals to communicate and activate the appropriate action.

Microcontroller processors often have a reduced instruction set computing (RISC), a limited number of bit words in their processing core and are provided with a small memory.

The key requirements for the microcontroller in the intended application, are the read refresh rate of the ADC, and the capability to process and store the information allowing a continuous throughput of data to the larger wearable memory (i.e., hard disk).

3 FR2 sensor RF front-end simulations, design, and verification

When targeting the FR2 band, the losses arising from the interconnection between the antenna and the sensing unit, strongly limit the available dynamic range of the sensing node. This thus requires a careful modelling and simulation approach to be carried out. When moving the down-converting unit in close proximity to the antenna interface, the sensing dynamic range can be maximized, by minimizing the detrimental effect of interconnection (i.e., cabling) losses. Moreover, when employing square-law detectors, the power consumption can be greatly reduced, thus enabling a deployable, low-cost and low-power sensor.

In [7] the authors reported a square-law detector co-integrated with the antenna unit and digitizing element, enabling a low-power sensing node at FR2 frequencies.

Nevertheless, the achieved dynamic range (DR) of the system, close to 40dB, would not enable to employ this unit as a deployable sensor to measure EMF radiation in urban environments, following the discussion of Section 2.2.

In this section, we summarize the design methodology and the preliminary result of a sensor node, based on the architecture of [7] but including a low-noise variable gain amplifier (VGA) to increase the dynamic range of the unit up to 60dB. Moreover, to reduce the assembly imperfection of the dual-polarized unit based on a Vivaldi antenna, a lens-based dual-polarized antenna, based on the work reported in [8], is selected, and its optimization for the given application is discussed in the following sections.

3.1 High DR detector simulation and validation

3.1.1 System and components

The electronic circuitry of the developed high DR sensing node is based on an LNA (QPA2628 [10]), digital step attenuator (ADRF5731 [12]), RMS power detector (LTC5596 [6]), and high-resolution voltmeter.

The LNA-first topology allows to set the noise figure of the detector close to the value of the LNA, i.e., circa 1.7dB, as was discussed in Section 2.2.

The 40dB digital step attenuator in combination with the circa 20dB gain LNA and the -40dBm input noise limit of the detector is designed to provide a ~60dB (reconfigurable) DR sensing node.

The prototype of the proposed sensing node RF front-end is shown in Figure 7.

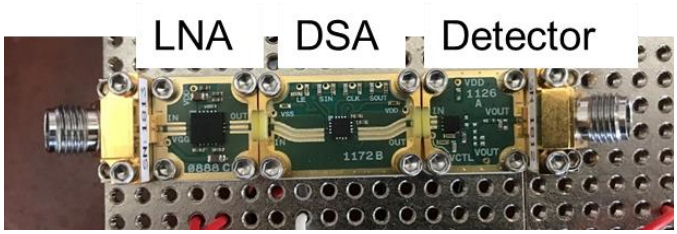

Figure 7: Prototype realize in the X-microwave technology of the proposed high DR reconfigurable sensing node.

3.1.2 ADS test bench

To evaluate in detail the performance of this system and accurately quantify the sensitivity and the readout uncertainty of the sensor, a test bench was developed in the Keysight advanced design system (ADS), see Figure 8.

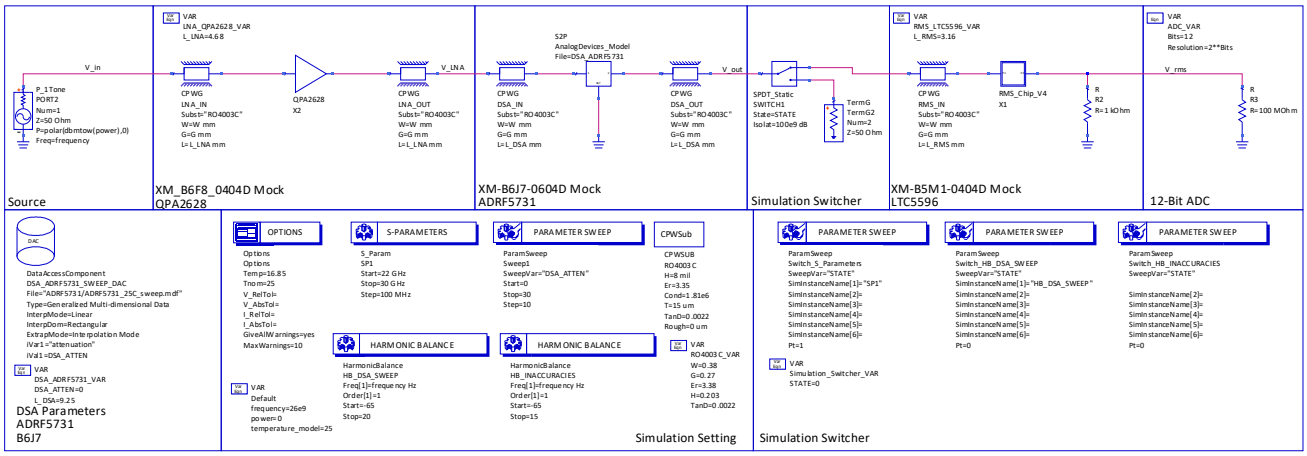

Figure 8: ADS test bench for FR2 sensor analysis.

3.1.3 Inclusion of component responses from datasheet

When attempting to perform an accurate system analysis/optimization, including both the signal conversion as well as the noise propagation, accurate models of the various components are required. Given the large frequency band operation of the FR2 telecom systems, each component to be simulated must also be accurately modelled versus frequency for their linear, non-linear and noise behaviour. Manufacturers often provide only S-parameters as downloadable information, while the other parameters are only mapped in the datasheet. In the employed test bench behavioural models from ADS, have been realized. These models can directly incorporate the S-parameter responses from touchstone files (provided by manufacturers). In addition, to correctly map the frequency behaviour of the noise figure and compression parameter, the following approach was employed:

1. A software tool to extract ASCII data from graph images was first employed.
2. The table of values is then converted into a generic MDIF file using Matlab scripting.
3. Finally, a data access component (DAC) in the ADS schematic was employed (see Figure 8, bottom left) to map the correct frequency dependency of the noise and non-linear parameters.

The proposed approach enables to incorporate in the simulation of an accurate frequency behaviour of the various parameters of each component used in the test bench, completely mimicking the data-sheet characteristics, as can be seen in Figure 9 a) and Figure 9 b). Moreover, the test bench allows to evaluate also the large signal response of the system as shown in Figure 9 c).

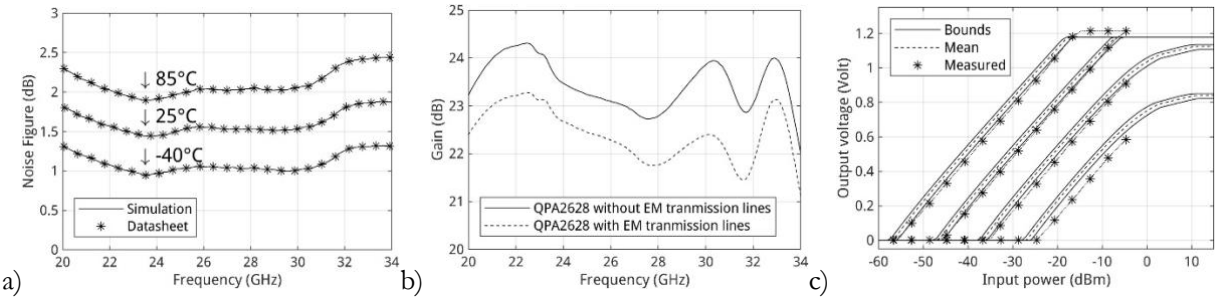

Figure 9: Simulation and measurement results: a) noise figure of the QPA2628 from datasheet and simulation overlaid, where the solid line is the datasheet values and the starred line is the noise figure of the amplifier in ADS; b) comparison of the QPA2628 model with and without transmission line losses; c) output voltage of the design vs input power in dBm, where the solid line is the simulation and the starred line is the measured response.

3.1.4 High-frequency EM response of the board environment

The frequency response of the active components needs to be further complemented by the EM response of the board-level interconnections. This is especially important at high frequencies (i.e., FR2 band) since the transmission lines between the components have non-negligible losses and frequency dispersion effects. Design files are not readily available from the component manufacturer or the company integrating the components in prototyping platforms (Quantic X-microwave). However, pictures of the layouts can be found on the prototyping platforms company for each component, as can be seen in Figure 10 a).

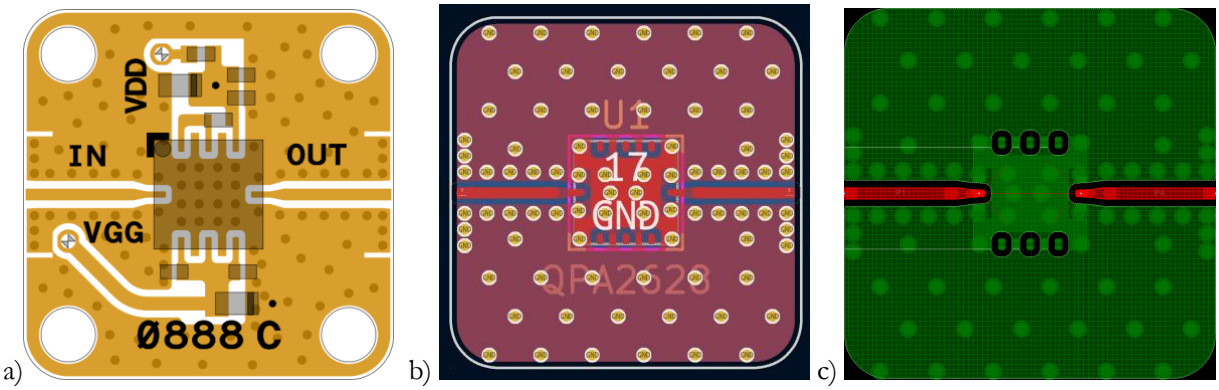

Figure 10: The different stages of converting the QPA2628 layout to a complete EM simulation; a) X-Microwave layout, b) Kicad PCB layout, c) ADS momentum layout.

Combining this image with the known dimensions of the X-Microwave blocks allows the creation of vector-based files to be imported into an EM simulation environment, i.e., Keysight Momentum, as shown in Figure 10 c).

To realize this conversion, the CAD program Freecad was used to import and scale to dimension the layout image. Once the image is properly set to scale, the transmission lines and vias can be drawn in the CAD program. The drawing can then be exported as DXF to be further elaborated into a program like Kicad, as shown in Figure 10 b). This approach isn't accurate enough for mmWave applications and thus the exact dimensions of the transmission lines need to be fine-tuned to match the datasheet performance, i.e., 50 Ohm.

This is due to the resolution of the image in conjunction with image compression. Within Kicad, vias can be added, and general placement of the transmission lines and copper opening can be drawn. From this environment, a Gerber file can be exported, which can then subsequently be imported into ADS momentum to perform the EM simulations. After the various components from the X-microwave library are imported and EM simulated, the data can be added to the test bench to improve the model-to-hardware correlation.

Adding the EM-simulated transmission lines to the model of the LNA (s-parameter response) shows the importance of this extra step. Figure 9 b) shows the drop of gain of the QPA2628 of circa 0.8 dB at 26 GHz due to transmission line losses.

After the completion of the test bench circuit and the assembly of the hardware block in the X-microwave technology to realize the sensor unit, the prototype of the electronic part of the sensor node was measured.

The characterization approach was based on the approach presented in [13], where the absolute power from a commercially available power sensor can be transferred to a vector network analyzer (VNA). This allows to employ the large dynamic range of this instrument (i.e., circa 100dB) to measure the power provided to a device under test (DUT), in this case the sensor unit described in the previous section.

The experimental data acquired is then compared to the simulation result from the test bench in Figure 9 c), indicating the good predictive capability of the developed test bench.

3.2 Lens antenna design and simulation

In order to minimize the distance between the antenna interface and the LNA, which is beneficial for the sensitivity of the node as discussed in Section 2.2., a PCB-based antenna was selected, with the electronic components (i.e., for the conditioning of the high-frequency signal and its digitization) placed in the opposite face of the PCB panel.

Moreover, to allow high flexibility in the antenna gain parameter required to support the different implementations of the sensing node elements into the various envisioned applications, i.e., static and wearable node architectures, a lens antenna topology was chosen.

In such topology, the feed element to the lens can be kept constant (not requiring any PCB redesign), while the overall antenna gain can be (within a reasonable range) tuned only by varying the lens dimensions (which can be quickly fabricated when 3D printing approaches are chosen).

To comply with easy implementation and fabrication, a direct contacting lens over the feed topology was selected, as sketched in Figure 11.

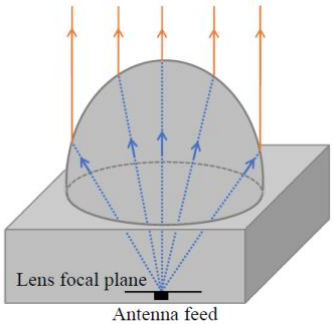

Figure 11: Lens antenna with integrated feed.

For the envisioned sensor, the dual-polarized leaky-wave fed lens antenna, developed in the TeraHertz Sensing section at the Delft University of Technology by the group of Prof. Nuria Llombart [8], was chosen.

The stratification of the PCB to realize the leaky-wave-fed lens antenna is shown in Figure 12 a), while Figure 12 b) shows the 3D CAD version to perform the full-wave EM simulation of the structure. This stratification and the dimension of the antenna elements were modified from the implementation of [8] for the following reasons:

- The new layer stack selected was identified with the PCB manufacturing company to minimize stress arising from differences in the thermal expansion coefficients of the layers in the original stratification.
- The antenna element and impedance matching were re-tuned to aim at the n258 band available in Europe for FR2 communication applications.

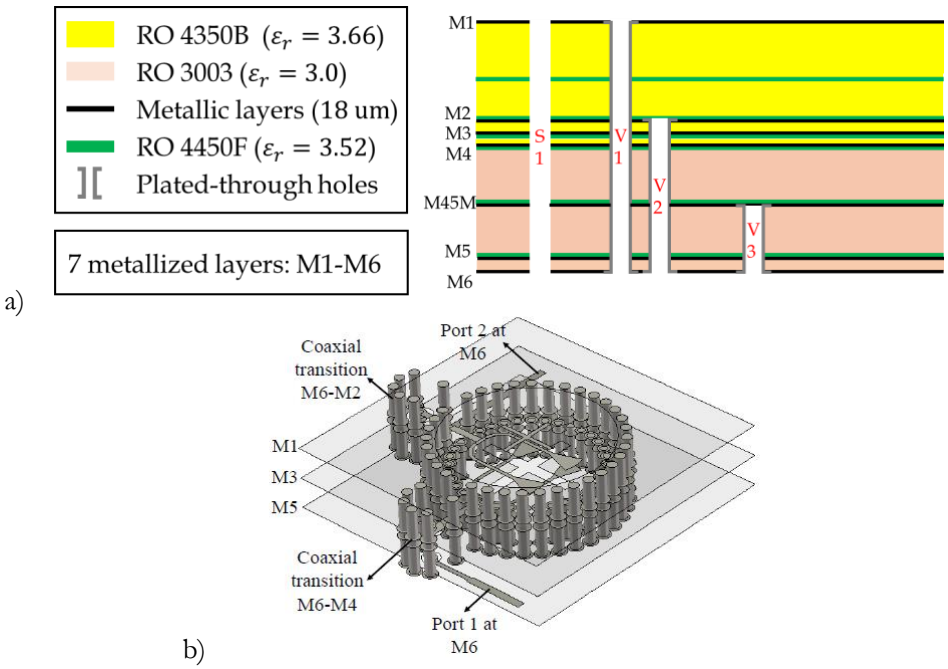

Figure 12: Dual-polarized leaky wave antenna feed: a) New PCB stratification, b) 3D perspective of the antenna structure from [8].

The structure was then simulated in the CST Studio Suite from Dassault Systems, to optimize the impedance match at the interface where the LNAs will be connected, i.e., port 1 and port 2 shown in Figure 12 b). The resulting input impedance for the two polarization and the feed cross talk are shown in Figure 13.

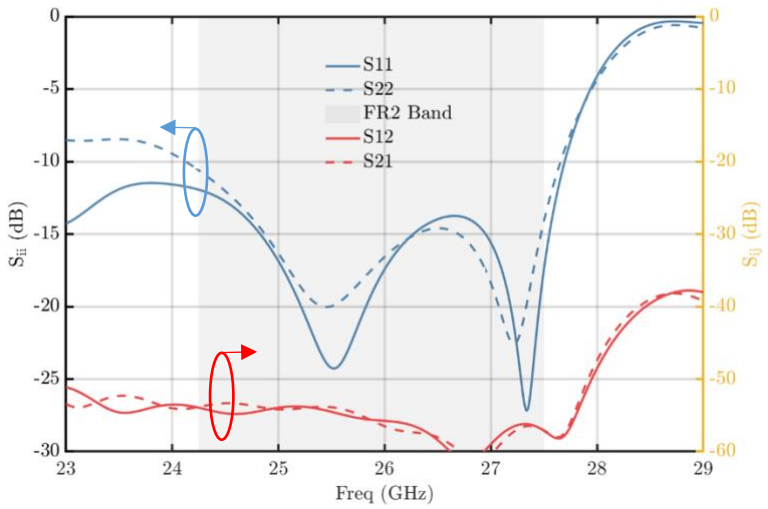

Figure 13: CST results of the input match at port 1 (S_{11}) and port 2 (S_{22}) from Figure 12 b), and the two orthogonal feeds crosstalk, S_{12} and S_{21}.

Once the input match at the antenna feed structure is tuned to reach the set specifications, the gain of the antenna can be, in first approximation, chosen by varying the diameter of the lens. The lens dimension of the front end for the FR2 sensor to be used in the use cases of WP7 was optimized to have low sidelobe levels in order to minimize the power coming from the direction outside the main angle of observation of the sensor.

The antenna patterns for the two polarizations are then shown in Figure 14, where also the diagonal (D, i.e., 45º) cut is added. The achieved side lobe level is close to -20dB providing very little power contribution to the sensed value for these off-beam directions.

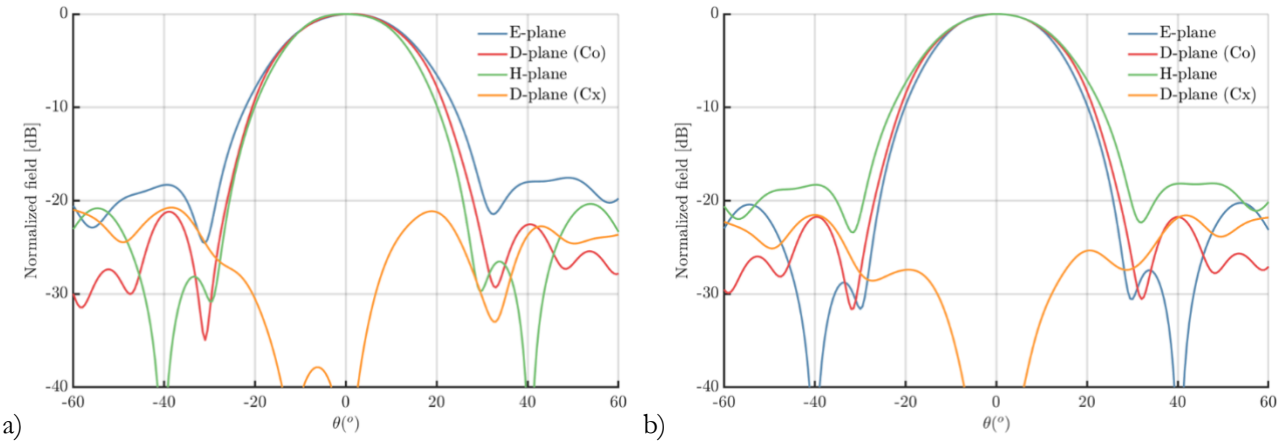

Figure 14: E and H plane full wave simulation including the plastic lens for the designed FR2 antenna front-end for a) polarization port 1, b) polarization port 2.

The lens shape can be then computed based on the geometrical and electrical parameters, as shown in Figure 15 a) and a 3D geometry can be realized and sent to the 3D printer, (Figure 15 b).

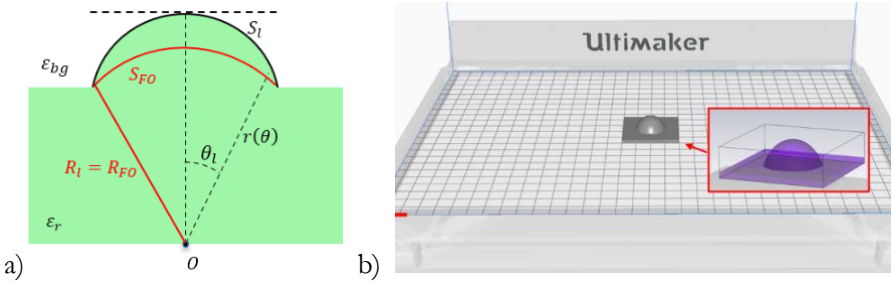

Figure 15: Geometrical dimensions of the lens, computed from the phase centre O, and related to the electrical parameters and diameter of the lens; b) computed lens geometry mapped into a 3D shape and sent to the printer (Ultimaker) for fabrication.

3.2.1 3D printed Antenna prototypes

As discussed in the previous section, the lens to focus the beam of the antenna feed is chosen to be realized using 3D printing technology. Conventionally, high-performance lens antennas use low-loss material which can be machined to realize the required shape. The realization of the lens presented in [8] employs high-density polyethylene (HDPE). While achieving higher performance, the material and the processing technique are less applicable for low-cost sensors. In order to identify the material to be used in the proposed approach, two filaments easily available in 3D printing technologies are considered and compared with HDPE, as shown in Table 2.

Table 2: Comparison of material electrical and mechanical performance.

Material	Density (g/cm³)	Permittivity	Electrical resistivity Ω · cm	Surface resistance Ω
HDPE	***0.924 – 0.995***	***2.10 – 3.00***	***1e+05 - 1e+17***	***10000 - 1e+14***
PLA	1.00 – 3.41	1.51 – 2.70	1e+08 - 1e+15	1e+10 - 1e+15
ABS	0.882 – 3.50	2.70 – 3.50	1500- 1e+18	1000 - 2e+17

Given the large variability of the material based on their impurity concentrations, and the density based on the infill setting of the 3D printing process, see Figure 16, an experimental evaluation of the permittivity of the available filaments with two different infill percentages was carried out, see Figure 17.

Figure 16: 3D printing infill patterns.

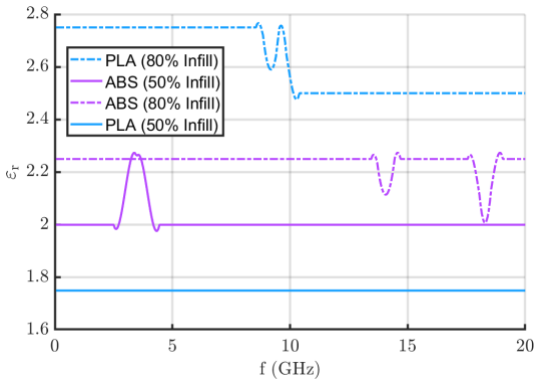

Figure 17: Measured permittivity for the PLA and ABS filament available at the XG labs at the Delft University of Technology for 50% and 80% infill. The small steps are arising from small gaps between the open-ended coaxial probe and the sample during measurement.

After the characterization an ABS filament with 80% infill was chosen, given the close similarity with the HDPE used in [8], providing an ε_r=2.34.

Two samples of the lens were realized using the ABS filament and are shown in Figure 18.

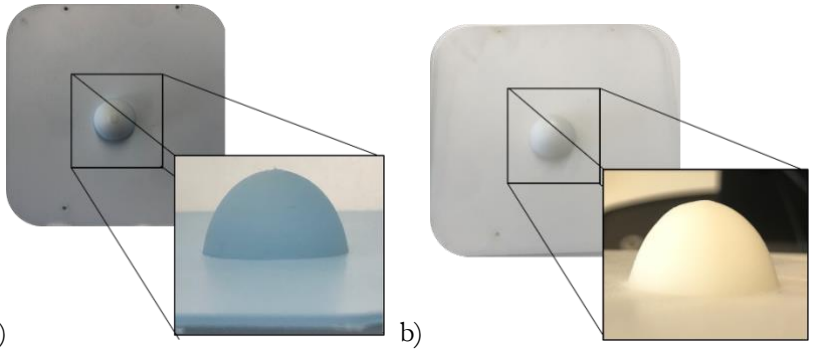

Figure 18: Lens antenna prototypes using ABS material with 80% infill, a) blue ABS, b) white ABS.

3.2.2 Final board environment including Lens and Electronics

The board stratification form in Figure 12 was then used to integrate both the radiating interface and the electronic signal conditioning in one boar; this resulted in:

- The top face of the board, see Figure 19 a), where the dipoles of the lens antenna are visible.
- A button face of the board, see Figure 19 b), where the footprints to solder all the electronic components to realize the HR detector described in Section 3.1 are present.

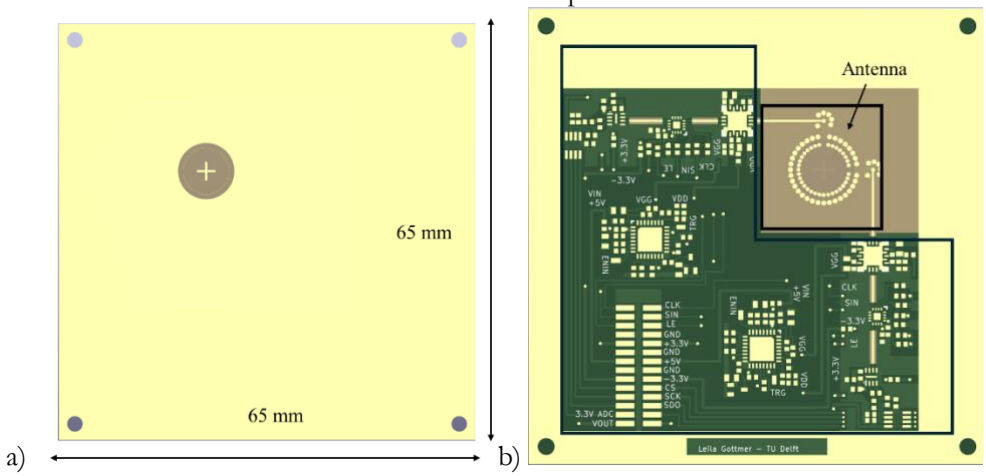

Figure 19: PCB board of the FR2 sensor integrating the lens antenna and the HR detector, a) front side (radiating/receiving side), b) electronic components and interface side.

On the backside of the board, both RF components, namely the biasing circuitry for the LNA and the SMD components (resistors and capacitors) for the biasing of the various active components, are embedded.

The board is designed for two modes of operation:

1) Static deployable sensor, discussed in Section 4.1: here the analogue (low frequency) signal after the RMS detector is routed to the 28-pin connector located on the bottom left corner of the board. This allows to route a large number of outputs to a single high speed digitizer unit in a high processing power microcontroller.
2) Wearable sensor vest, discussed in 4.2: the output of both the RMS sensors (each for one of the polarizations) are directly digitized on the board using a 12-bit 500ksps controlled via an SPI interface using the microcontroller board discussed in section 3.3. This configuration is preferable in the vest environment where the capability to integrate a high-power processing unit is not feasible due to power budget constraints.

Finally, in Figure 20 the cross section of the board is shown, highlighting the vias (i.e., vertical interconnections between different metallization layers) complexity and the different environments, i.e., antenna interface, distribution and bias domains.

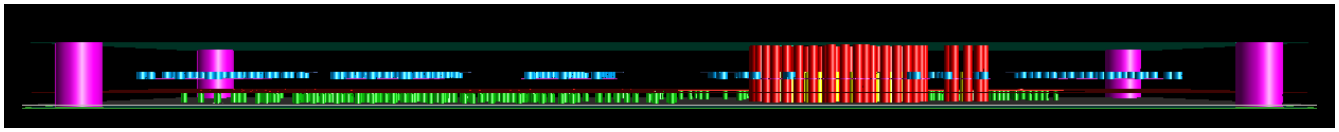

Figure 20: Cross section of the board: red vias defining the antenna cavity area, green vias to provide low inductive connections to the RF distribution, blue vias allowing for low frequency signal distribution, large pink vias for mounting and assembly.

3.3 ADC, Microcontroller system verification

As was discussed in Section 2.3 the microcontroller needs to provide the (data) interconnection, the processing capabilities, the temporary storage, and interface with the central unit of the network of sensors embedded in the vest, see Section 4.2.

For the chosen sensing node, a compact microcontroller board was developed, see Figure 21. The sensor node can be controlled, from the board, through an SPI [9] interface, other interfaces such as digital, analogue, I2C or UART are available for future extensions if required. The supply voltage can be either 3.3 or 5 V.

Figure 21: MCU board 3D image generated from KiCAD detailing the different component to be soldered, the USB connector and the vias area to allow easy interface with additional boards.

A software framework has been developed for the sensor node that is capable of reading the ADC, filtering the samples and pre-processing the data when necessary. The data collected in this way are then made available to a logging system on the wearable vest via a proprietary protocol, discussed in Section 5.2. The requirements for the microcontroller are:

a) Inclusion of a hardware SPI interface to communicate with the ADC and capable of achieving a sample rate of at least 10000 samples per second.

b) Random access memory (RAM) to store at least 100 consecutive floating-point samples.

c) Read only memory (ROM) to handle acquisition, scaling of samples, non-volatile memory for storage of the configuration, a look-up table for calibration (100 entries), and the communication protocol with vest.

A rough estimation of the resources needed resulted in the following minimum requirements:

a) Peripherals: SPI, UART, I2C, at least 2 timers.

b) RAM size of at least 1.5kB.

c) ROM size of at least 20kB and non-volatile memory of at least 0.5 kB.

In addition to the above requirements the peripherals should be able to handle 3.3 and 5 V signals, which will result in an additional level-shifter.

Other requirements of the microcontroller are low cost and good availability (in case of future high-volume production of the nodes).

The Microchip ATmega328PB [14] matched the requirements and was chosen to interface the sensor. The ATmega328PB provides the following specifications:

- low-power 8-bit CMOS microcontroller based on an enhanced RISC architecture with 32 kB of in-System programmable flash-ROM for program storage,
- 1 kB EEPROM for configuration storage,
- 2 kB RAM,
- two 8-bit Timer/Counters with prescaler and compare mode,
- three 16-bit Timer/Counters with prescaler, compare mode, and capture mode,
- two serial ports providing synchronous/asynchronous communication (USART),
- two SPI serial interfaces,
- two I2C interfaces,
- 27 programmable I/O Lines (GPIO),
- operating voltage 1.8 – 5.5 Volt.

The selected ADC for the sensor board is the LTC2312-12 [15], a 12-bit, 500ksps, serial sampling A/D converter that draws 3mA from a single 3V or 5V supply. The 12-bit resolution, with a reference voltage of ~2V, guarantees an LSB quantization level well below the output noise floor of the selected RMS detector, fulfilling the criteria defined in Section 2.3.

3.3.1 Microcontroller Logger data flow

The logging system consists of two levels of hierarchy, first at the end sensor nodes connected to the antennas and then at the central node which polls at a certain interval for the data from the sensor nodes. The sensor node collects the time-averaged antenna power over a second and central node, which in turn retrieves and stores the

data from the nodes in its local storage. In the following Sections, we describe the data flow design on the sensor nodes and the central node in detail.

Sensor node:

The sensor node is designed to respond to the commands from the master node and also to continuously poll the RMS detector to measure the antenna power. The power from the antenna computed by the RMS detector is fed to the sensor node via an external ADC interfaced together using the SPI protocol. The sensor node periodically samples the ADC at 200 µs to capture the antenna power in dB from the RMS detector using the ADC. The antenna power needs to be averaged over a one-second duration to compute and store metrics for the average exposure level. However, the antenna power measured in the dB scale cannot be directly averaged over a period of time since it is in a logarithmic scale and requires it to be first converted into the linear scale and then averaged. To convert the antenna power in the logarithmic scale into a linear scale, we have a few possible approaches, which are as follows:

A. Obtain the logarithmic relationship between the input antenna RF power and the output of the RMS detector (LTC5596) using the relationship curve from the datasheet as shown in Figure 22 a), from which the antenna power in mW can be computed using log function from the standard C library.
B. A lookup table is used to show the relationship between the ADC voltage and the corresponding linear power in mW.
C. Using a predetermined polynomial relationship that relates the received linear antenna power in mW to the output voltage of the RMS detector.

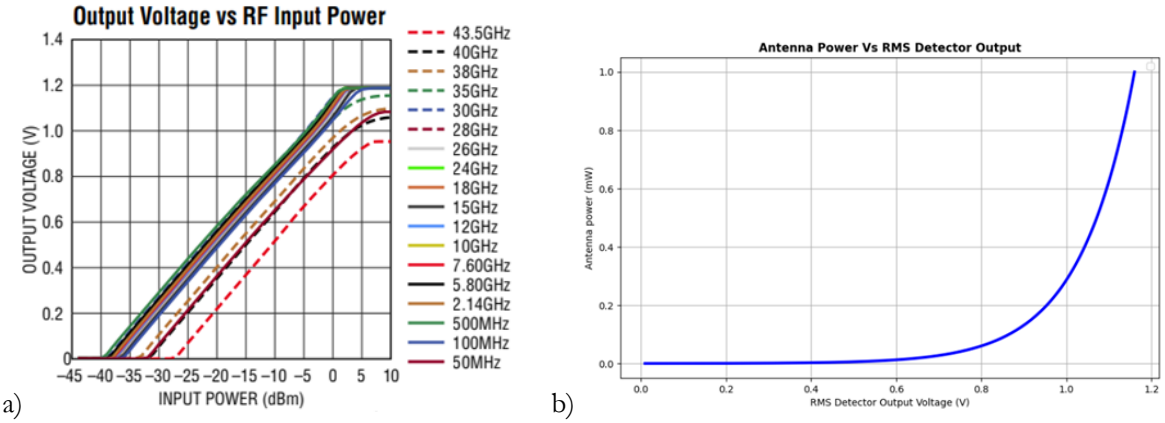

Figure 22: a) Output voltage of the LTC5596 RMS detector vs input RF power from the antenna in dB scale from the datasheet; b) output voltage of the LTC5596 RMS detector vs input RF power from the antenna in mW scale obtained via experimentation.

We used the polynomial relationship based on experimental calibration because it has higher accuracy that relates to the experimentally obtained power curve from the actual antenna that was used in the setup and also because it can be computationally advantageous. In order to derive the polynomial relationship that corresponds to the received power in linear scale with respect to the voltage from the rms power detector, a least squares approximation was used. It can be noted that the least squares approximation approximates a function *g* close to our experimental antenna power values in linear scale given by the function *f* within a, b $\in X$ such that the error $\|f - g\|$ is minimised in L2 space, represented as follows.

$$\|f - g\| = \int_a^b \big(f(x) - g(x)\big)^2 dx$$

g(x) is approximated as a polynomial such as

$$g(x) = \sum_{i=0}^{N} \alpha_i g_i(x)$$

It was found that the least squares approximation for our antenna function was able to converge at the 11th-order polynomial with a mean and maximum error of 0.063% & 1.67% between the actual function and the approximated function. It should be noted that the convergence at the origin improves as the order of the polynomial is increased, which can be demonstrated in Figure 23, which compares the original function with the approximated function for the 7th and 11th order polynomial.

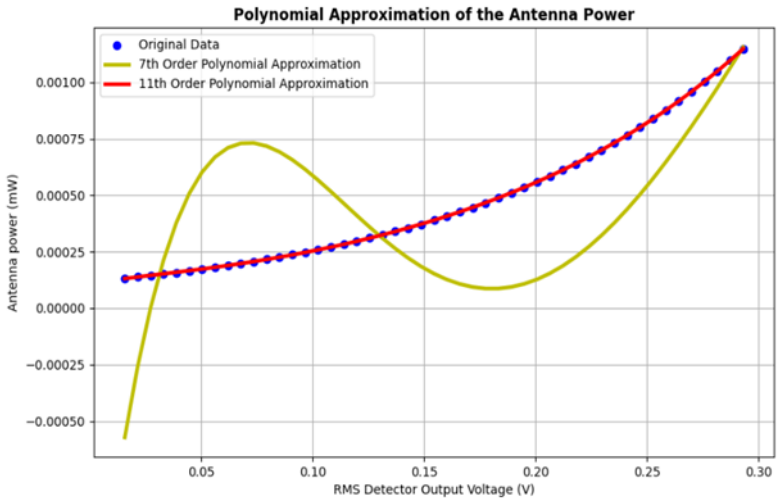

Figure 23: Polynomial approximation of the antenna power at the origin with a 7th-order polynomial and 11th-order polynomial. It can be observed that there is an error between the original data and the 7th-order polynomial, whereas the 11th-order approximation has a better fit with the original data.

It can be noted that the number of floating-point additions and multiplications varies according to the order of the polynomial N given by the relationship 2N-1 and N, respectively. For instance, for the 11th-order polynomial, we require 21 floating point multiplications and 11 float point additions. As the order of the polynomial increases, the number of floating operations increases, which would, in turn, increase the computational time such that it would have an impact on the rate at which the power can be measured or sampled. Optimization of the algorithm was required for our low-cost embedded microcontroller that did not have a hardware floating point support and a maximum clock rate of 16MHz in order to ensure that the power averaging is performed at intervals of at least 200µs.

In order to improve the algorithm, we can reduce the range of the function over which the LS approximation is performed. We choose c, d $\in Y$ such that they are subsets of a, b or $Y \subseteq X$ where c and d are the limits of integration for the LS error function. On reducing the limits of integration, the area of function f that needs to be approximated with the polynomial of order N is reduced since the function f is continuously increasing under the interval a, b. Since the LS error is reduced, it can be possible to find a lower order polynomial M that can approximate the function f over c, d with an error comparable to a polynomial of higher order N approximated with the function f over a, b. These properties can be represented by the following equations.

$$\|f-g\| = \int_a^b \left(f(x) - \sum_{i=0}^{N} \alpha_i g_i(x) \right)^2 dx$$

$$where\ a, b\ \in X;\ c, d\ \in\ Y; Y \subseteq X$$

$$\|f-g\|\ \geq \int_c^d \left(f(x) - \sum_{i=0}^{N} \alpha_i g_i(x) \right)^2 dx$$

$$\|f-g\|\ \geq \int_c^d \left(f(x) - \sum_{i=0}^{M} \alpha_i g_i(x) \right)^2 dx$$

$$where\ \mathrm{M} \leq \mathrm{N}$$

It implies that we can find a polynomial of order M such that the error is limited within $\|-g\|$, which implies that, lower order polynomial could be found such that it be able to generate the error comparable to the higher order polynomial which approximated the original data across the entire range a, b. In our system, we segmented the function into 5 segments and used the LS approximation in the individual segments. It was observed with the data segmentation approach that the mean and maximum error for approximating our function with a 3rd-order polynomial was found to be 0.2% & 1.12% with respect to the actual values, which is sufficient for the system. Computing a 3rd-order polynomial requires 5 floating point multiplication operations and 3 floating-point addition operations, and a maximum of 4 integer comparison operations for finding the segment in which the data point is situated. It should be noted that floating-point multiplication and addition are costly operations for

microcontrollers without a hardware floating point unit (FPU) such as ours that would result in software floating-point implementations by the compiler, which would cost several cycles. An integer comparison operation is a simple computation operation that can be computed within 1 hardware cycle that is significantly faster in comparison to floating point operations. In our optimization, we managed to reduce the floating-point multiplications from 21 to 5, a 4.2 times improvement and floating-point additions from 11 to 3, a 3.6 times improvement, with an additional minimal overhead of up to 4 integer comparison operations.

Central Node:

The central node shown in Figure 24 is a Raspberry Pi Zero 2W that has wireless WiFi capabilities and a Linux OS that offers several functionalities that are suitable for data collection, data storage and transfer of data using a LAN network for real-time and offline connectivity. The central node is connected to 4 sensor nodes corresponding to 2 orthogonal antenna pairs, via a USB connection that uses a serial terminal UART protocol at a 9600 baud rate. The sensor node is configured to respond to certain commands for sending sensor data, which are used by the central node to retrieve the antenna power data periodically at intervals of 1 second.

The software is written using Python for its simple syntax and the wide availability of libraries that allow faster development, scalability and easy maintenance. On start-up the software checks for the available nodes that are connected to the system and registers it into a list. It then polls the connected sensor nodes sequentially once a second for collecting the data and stores the data with a timestamp from the local time in a predefined directory structure mapped in the local SD card file system. Furthermore, the system is configured as an SSH server with static IP settings that can automatically connect with a predefined router network such that it can be accessed by the user to retrieve the data or change parameters in the software.

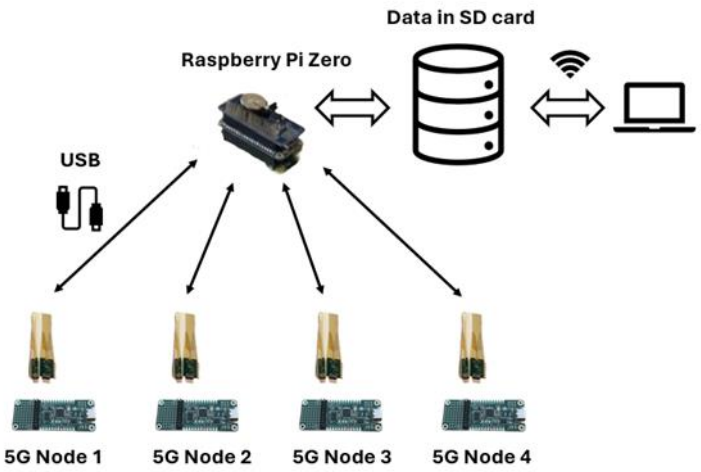

Figure 24: Representation of the data flow between the 5G sensors to the central node that collects and stores data in the SD card and that can be accessed or retrieved using WiFi connectivity.

3.3.2 First experimental tests

First the performance of the RF front-end with the ADC converter were tested. A similar test bench to the one employed in Section 2.1 was used. Now the data was acquired directly with the LTC2312-12.

The characterization results are shown in Figure 25, where the achieved DR (~57dB) is reported.

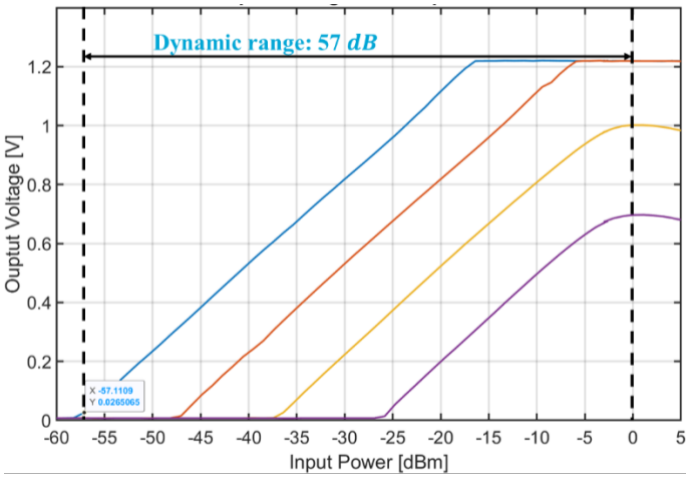

Figure 25: Measured dynamic range of the prototype realized in the X-microwave from Figure 7 with the LTC2312-12 ADC. The same VNA-based test bench discussed in Section 3.1 was used for the characterization. A maximum DR of 57dB is reported.

Subsequently, the ADC microcontroller interface was tested to evaluate the effective speed and resolution that can be obtained. The block scheme of the circuit used for the test is shown in Figure 26.

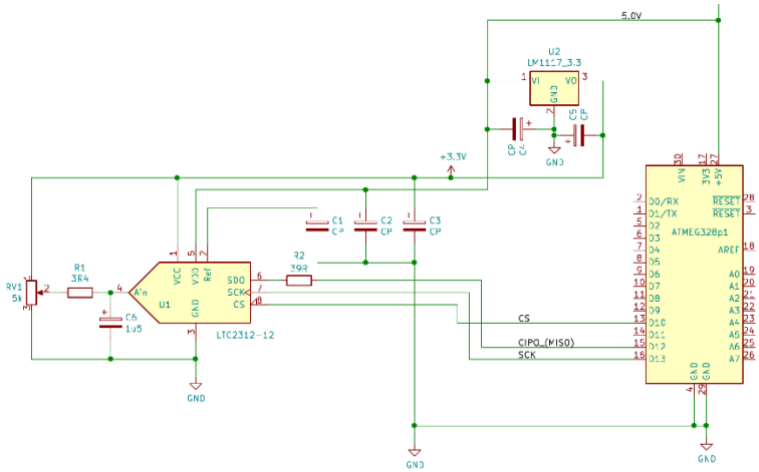

Figure 26: ATmega328p and LTC2312-12, the AVR-GCC compiler is used to read from the microcontroller.

Running the MCU at 16MHz clock and reading the ADC with the 8MHz SPI clock resulted in an acquisition time of ~8 µs, as can be noted in Figure 27, considering the overall time where Channel 2 is low.

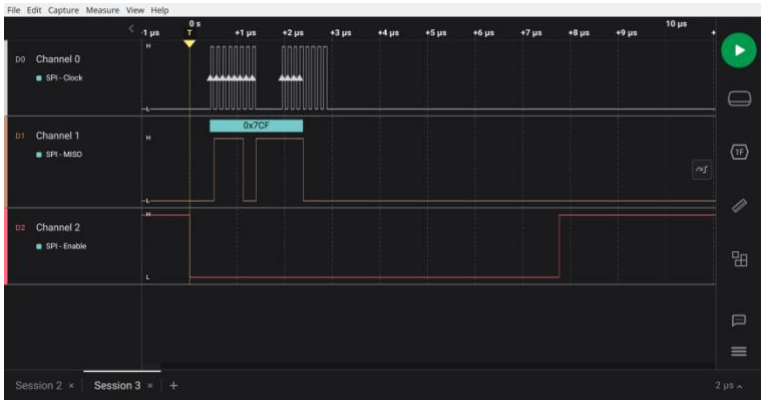

Figure 27: Acquisition of a single 12-bit sample shown in the Channel 1 trace.

Figure 28: 64 samples acquired (Channel 1 trace) in less than 1ms (SPI-clock of 8MHz, Channel 2 trace).

Acquiring 64 consecutive samples gave an overall acquisition time of less than 1 ms (Figure 28). The oscillograms of a single acquisition are shown in Figure 29.

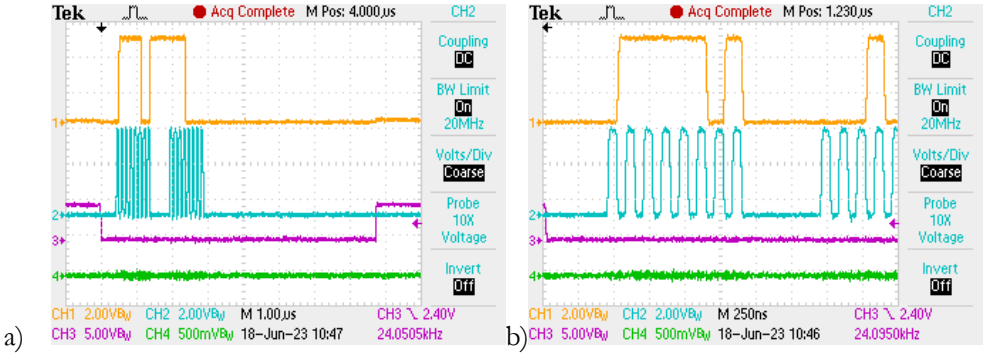

Figure 29: a) Total acquisition-cycle, b) Reading 12 bits only. (CH1 SPI-Data orange, CH2 SPI-Clock turquoise, CH3 SPI-ChipSelect purple, CH4 Noise on power-supply with 20MHz bandwidth green)

An acquisition of 64 samples within 1ms is possible, which does not include further additional data processing. This will be sufficient for a sample-rate of at least 10000 samples per second as required, leaving enough time for communication and data processing.

Due to the high possible acquisition rate of the ADC itself (500ksps) and the USART acquisition method, great care has to be taken when designing the power-supply of the device to avoid noise and to guarantee failure-free operation.

3.4 OTA testing first prototype

The antenna front end with the 3D printed lenses discussed in Section 3.2.1 were tested for their performance at the EMC XG labs at the Delft University of Technology.

3.4.1 Planar near-field test bench for antenna performance characterization

The near-field characterization setup, designed at The Delft University of Technology, senses the field over the antenna under test (AUT) by scanning a probe (receiving) antenna over a planar surface (planar near-field) at a given distance from the antenna plane, as shown in Figure 30 a). One port of the VNA is connected to the AUT and provides the feeding to the antenna.

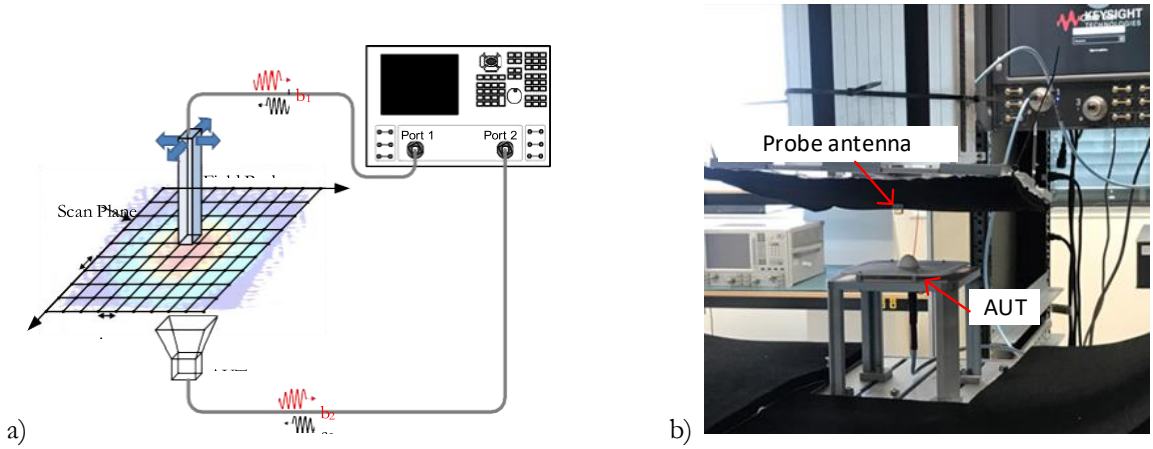

Figure 30: Near-field antenna measurement setup: a) schematic representation, b) implementation at the EMC XG labs at the Delft University of Technology [17].

The other port of the VNA is connected to a field probe antenna, in the considered setup an open-ended waveguide (OEWG) operating in the WR28 waveguide band.

The probe antenna is mechanically scanned throughout the plane using a computer numerically controlled machine. The measurement is performed in the radiating near-field of the AUT [18]. The mechanical movement, performed by two linear stages, samples the near field above the AUT with a sampling interval of $\Delta x \leq \lambda/2$ and $\Delta y \leq \lambda/2$ to fully reconstruct the far-field pattern, where λ represents the wavelength in air at the maximum characterisation frequency of the antenna under test. The electric field is obtained from the measurement of the amplitude and phase of the $S_{21} = b_2/a_1$ parameter, being a_i and b_i the incident and reflected wave of port i respectively. These near-field points captured in the plane can then be translated to far-field patterns by performing a two-dimensional (2D) Fourier transform [18].

For the lens antenna characterization, 3D-printed holders, see Figure 31, were manufactured to provide a stable horizontal holder for the antenna panel and allow precise 45° rotation. This allowed us to compare the diagonal response of the radiation pattern accurately with the simulation results.

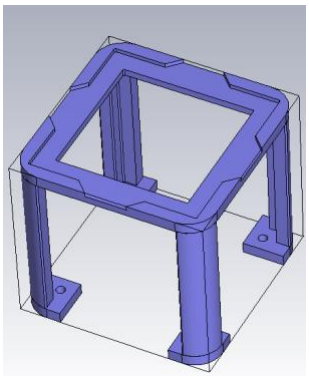

Figure 31: 3D printed holder to accurately position and rotate the antenna panel.

3.4.2 3D printed Lens antenna measurements

As discussed in the previous section the planar near field system acquires the field intensity, measuring the complex S21 parameter, over a plane located in the near field of the antenna under test.

For the measurement a distance of ~4 cm was used, and a scan area of 13.2 cm x 13.2 cm. The magnitude of the field is plotted for the 44x44 grid (using a Δx and Δy displacement of 3mm) in a dB scale and normalized to the centre element in Figure 32.

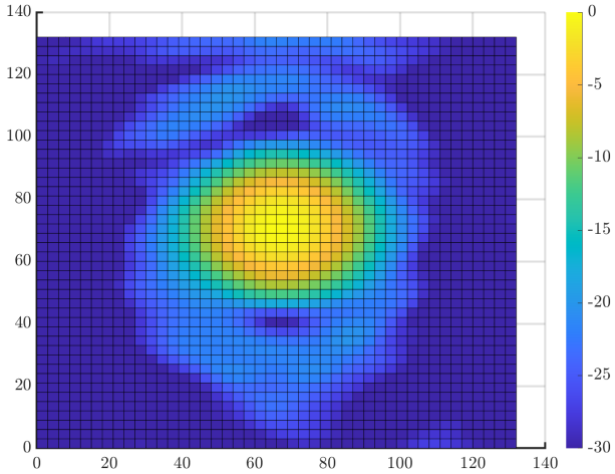

Figure 32: Magnitude of the sampled field expressed in dB scale and normalized to the centre element.

The acquired field is then processed with the developed near field to far field transformation to obtain the 3D far field pattern of the AUT and plotted in Figure 33 a) in the UV plane, while Figure 33 b) presents the 2D response over the E and H plane.

The measurement results show a good agreement with the simulation for the main beam and the side lobe level which was the design parameter optimized with the specific lens design.

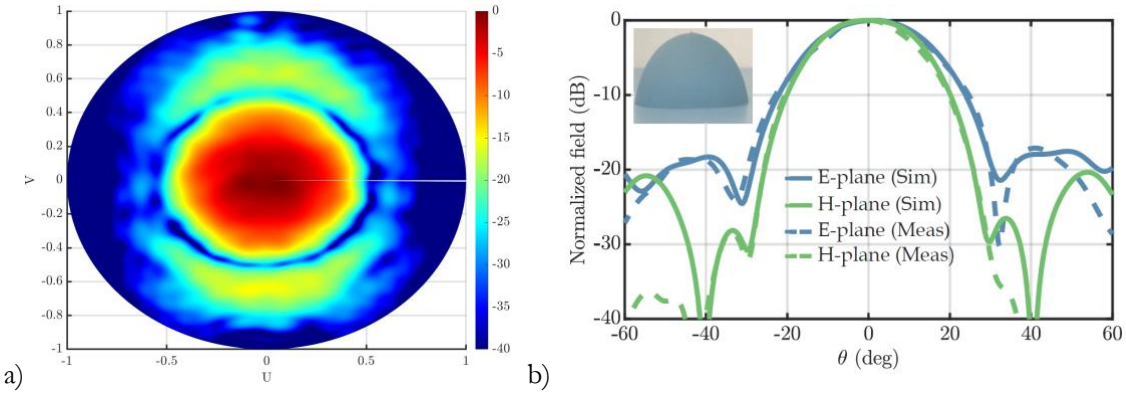

Figure 33: Measurement of the lens antenna after the near field to far field transformation, a) field intensity in the UV plane, b) normalize field for the E and H planes over the elevation angle.

3.4.3 High-speed characterization of the prototype sensor under different incidence angles

The fabricated PCB lens antenna sensor, discussed in Section 3.2.2 will be then characterized in a 3D environment "The Antenna Dome". This is a far-field system developed at the ELCA section of the Delft University of Technology [7][19], see Figure 34 a). The mechanical structure of the Antenna Dome is based on a geodesic anechoic dome skeleton, where 36 dual-polarized sensing nodes are distributed as shown in Figure 34 b).

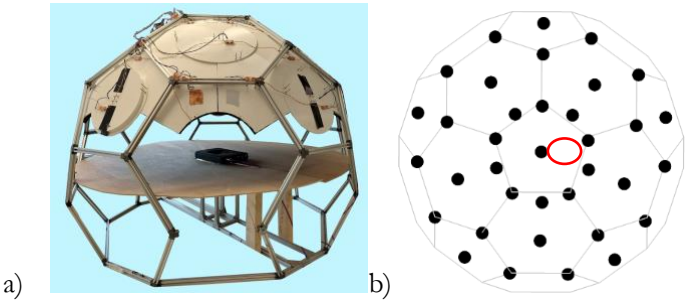

Figure 34: Antenna Dome with geodesic anechoic environment dome skeleton partially open to see AUT and wooden plate where base absorbers are placed, b) top view node nominal configuration in respect to the mechanical assembly.

The Antenna Dome provides the unique capability of performing full 3D antenna measurement in less than 100 ms. The antenna Dome will first be used to accurately characterize a 4x4 phased antenna transmitter module that will be further used in the prototype characterization. The prototype will be measured during two conditions:

1) The antenna interface of the prototype will be placed in place of the azimuth node of the Antenna Dome (see Figure 22 b) circled node). The pre-characterized phase array will be used to provide signals with known value, for different setting of the transmit module. The sensor will be then calibrated based on the a-priori information of the transmitted signal.
2) The prototype sensor will be placed in the centre of the dome and mounted on a two-axis Gimbal (see Figure 35). The azimuth node of the Antenna Dome will be replaced with a transmit unit, capable of providing a 26.5GHz signal to the prototype sensor. The Gimbal will be used to simulate different angles of arrival of the EMF field on the sensor in order to experimentally evaluate the angle of observation of the sensor.

Figure 35: Two-axis gimbal positioner from Newmark model GM-6.

3.4.4 5G compliant signal generation and up-conversion

In order to characterize the sensor response for 5G signals used in commercial gNodeB, a modulated standard compliant 5G signal was created in the NextGEM consortium and reported in D4.5, as shown in Figure 36.

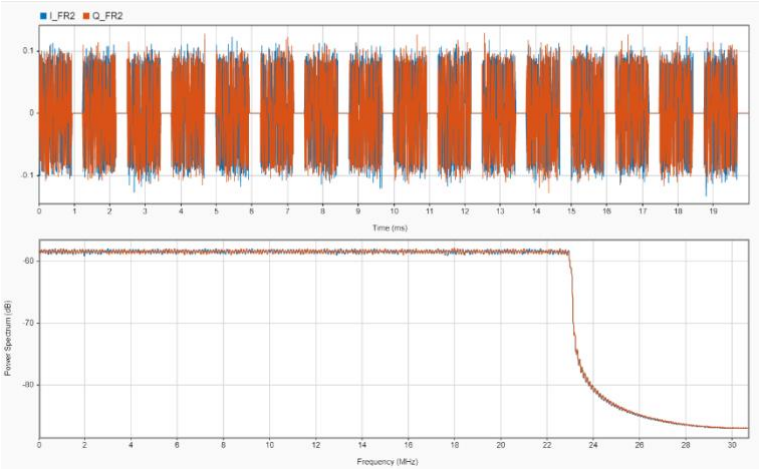

Figure 36: Time domain (upper plot) and frequency domain (lower plot) of the 5G NR signal generated by the NextGEM consortium, version 50MHz bandwidth.

Within the activities of Task 3, these signals have been mapped to the HW layer using a low-cost SDR solution, i.e., the Adalm Pluto, see Figure 37.

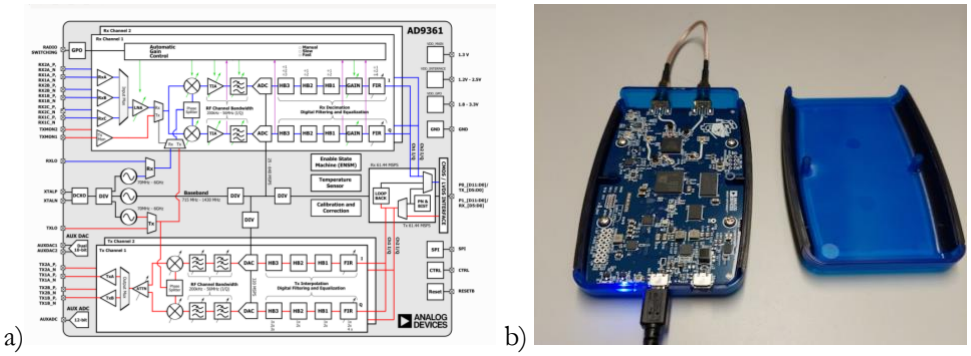

a) b)

Figure 37: Adalm Pluto SDR: a) internal block scheme, b) hardware assembly with the micro usb interface.

Finally, an upconverter to shift the modulated signal from the below 6GHz band (upper frequency from the SDR) to the FR2 band was realized in using the X-microwave fast prototyping platform, see Figure 38 a), and tested, see Figure 38 b).

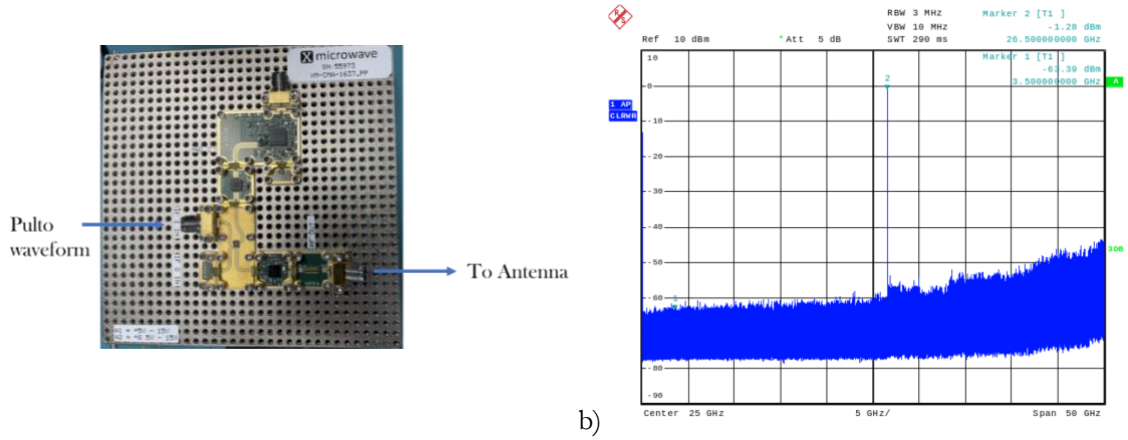

a) b)

Figure 38: a) Upconverter in X-microwave fast prototyping technology, b) upconverted tone at 26.5 GHz using the Adalm Pluto and the upconverter.

4 Monitoring methodologies using low power sensors

The FR2 node described in Section 3 and developed by the NextGEM partners in Task 3.3, forms the sensing unit for two system architectures used for exposure level monitoring in the use cases considered for Task 7.3, namely a static deployable node and a wearable one.

In the next sections, the design trade-offs arising from the specific implementation of the sensing node will be described, and the key performance parameters of the two different architectures will be identified.

4.1 Monitoring methodologies using static deployable nodes

As was discussed in [21], exposure to RF-EMF fields in real application environments is an important factor in better understanding the real network dynamics and deriving accurate statistics to accurately employ the extrapolation methods used in standardized measurements for exposure limit compliance.

The spatiotemporal monitoring is carried out by employing static deployable sensing nodes, covering the band of interest, in areas where signal coverage and network usage is present, see Figure 39.

a)  b) 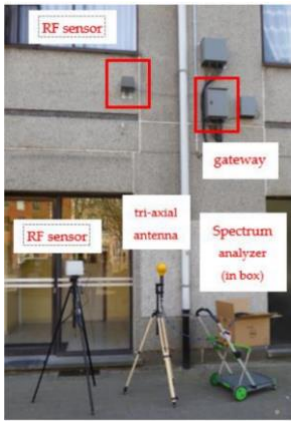

Figure 39: Sensor node from [21] in its casing, covering four different RF bands, b) static deployable sensor node and gateway mounted on building façade.

As was discussed in Section 3.2, the developed sensor makes use of high gain (lens-based) antennas to improve the overall system sensitivity. This choice reduces the solid angle illuminated by the antenna when used in transmit mode or, alternatively, the observed spatial region observed by the sensor when the antenna is employed in receiving mode, as is the case in the power sensor. This simple consideration highlights the need, when employing the developed sensor in the system architecture, to consider the usage of a multitude of sensing units to cover a larger (user-defined) spatial region.

In order to calculate the number of sensors needed for a given lens antenna topology, the following approach is employed:

1) The radiation pattern of the lens antenna employed in the sensing node can be approximated based on the lens dimension, using equation 4.1, computed for the case of a 2λ lens.

$$\theta_{HPBW} \approx \frac{\lambda}{D} = \frac{\lambda}{2\lambda} = \frac{1}{2}(rad) = 28.6° \quad (4.1)$$

This results in the radiation pattern as shown in Figure 40.

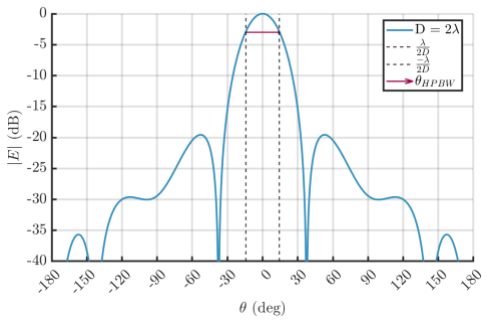

Figure 40: Radiation pattern of a lens antenna with diameter set to 2λ.

2) The half power beamwidth can be used to compute the number of beams (i.e., sensing nodes) over one radius to obtain a beam overlap of ~3dB, as shown by Equation 4.2 and Figure 41 a).

$$N_{beams} = \frac{180°}{\theta_{HPBW}} = 7 (when \theta_{HPBW} < 30°) \quad (4.2)$$

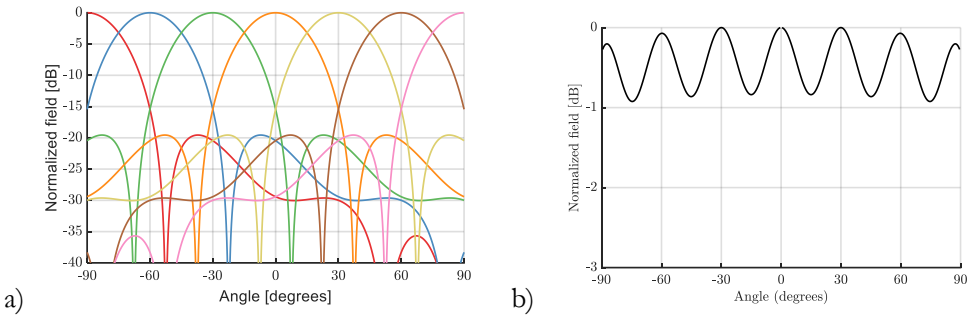

a) b)

Figure 41: a) Beam overlap between sensors equally spaced on a hemisphere with a normalized radius of 1, when each of the sensors is realized with a lens antenna with radiation pattern as shown in Figure 40; b) total field received versus angle when considering the number and disposition of sensor from Figure 41 a).

3) The number of sensors depends on the number of patterns required to realize the crossover (i.e., beam intersection) at a given level (i.e., -3 dB in Figure 41 a); this level depends on the value of the maximum deviation from the total power received from the surrounding hemisphere and the measured one, which the user can accept; an increase in the acceptable deviation allows a decrease in the level of the crossover points between the patterns, and therefore in the number of sensors needed.
4) When expanding the analysis from a 1D cut to a 2D surface, the location of the sensors can be placed over the hemisphere architecture, as shown in Figure 42 a), the radiation pattern of the lens antenna is consequently also scaled to a 2D one as shown in Figure 42 b), where the dashed curve represents the 3dB level.

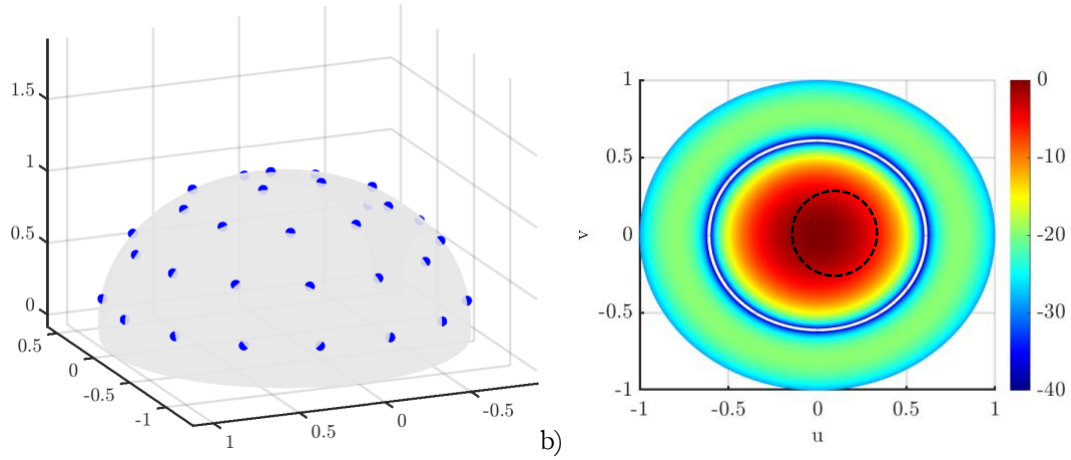

a) b)

Figure 42: a) positioning of the sensors over a (radius normalized) hemisphere to realize the beam overlap shown in Figure 41 a); b) 2D radiation pattern of sensor employing a lens antenna as in Figure 40.

4.2 Monitoring methodologies using wearable deployable nodes

When considering monitoring methodologies using wearable nodes, the sensing elements are deployed on a vest, see Figure 43, which is carried during the measurement campaigns.

For case study 3, the vest will have sensors at several positions on the body where either the incident field will be at the highest field strength or, depending on the outcome of the modelling exercise, where the incident field on the body may cause the highest internal electric field in the red blood cells in superficial blood vessels.

In general, the sensor vest will be applied as a distributed exposimeter measuring concurrently at multiple body positions to avoid body shielding in case the incident beam comes from the left side and the sensor is being worn on the right hip, thus not registering any field reaching the sensor on that side.

Figure 43: Measurement vest developed by the smart sensor system at The Hague University of Applied Sciences.

The distributed sensor system consists of a number of nodes registering the RMS power density of the incoming field at different positions on the body and a real-time clock (RTC) and GPS location concurrently. The number of nodes that will be used depends on various factors, among which the capability of the logging system to handle the large amount of data generated. At the time of writing, a minimum of four nodes (i.e., on the four cardinal points) is envisioned.

The sensor nodes are connected to the logging system via a low-cost USB interface, see Figure 44. This USB port supplies the sensor nodes with a voltage of 5 volts from a battery pack (power-bank), eliminating the need for separate batteries or accumulators.

By using readily available standard components, the costs for the overall system are kept low and the network is easily expendable with low-cost parts.

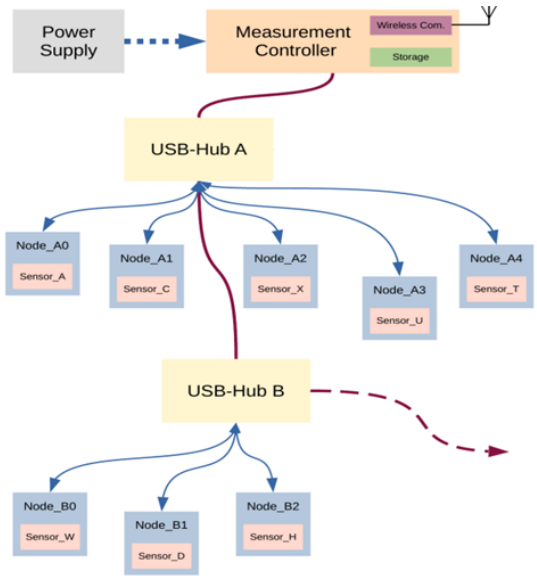

Figure 44: Overview of the logging system of the vest.

The software for the logging system is written in C++ and can be compiled and run on any UNIX-like platform. The system can be configured by a single external text file to access the available nodes. The data from each of the

sensor nodes can be collected at a rate of up to one reading per second. For easy access, the data from all sensor nodes is stored in a single text file (CSV format) in chronological order. Since the logging system is running on a UNIX-like platform, all of the features and capabilities of this operating system are available for retrieving the data and downloading it to any computer. It will be stored locally and transmitted by WiFi to the server once it comes into range. Also, the signal can be sent in real-time to a smartphone to give direct insight into the local exposure situation.

In the wearable deployment case, the full hemisphere coverage using an architecture as described in Figure 42 a) is not practical; for this reason, a simple ring architecture is chosen for modelling this use case, as sketched in Figure 45.

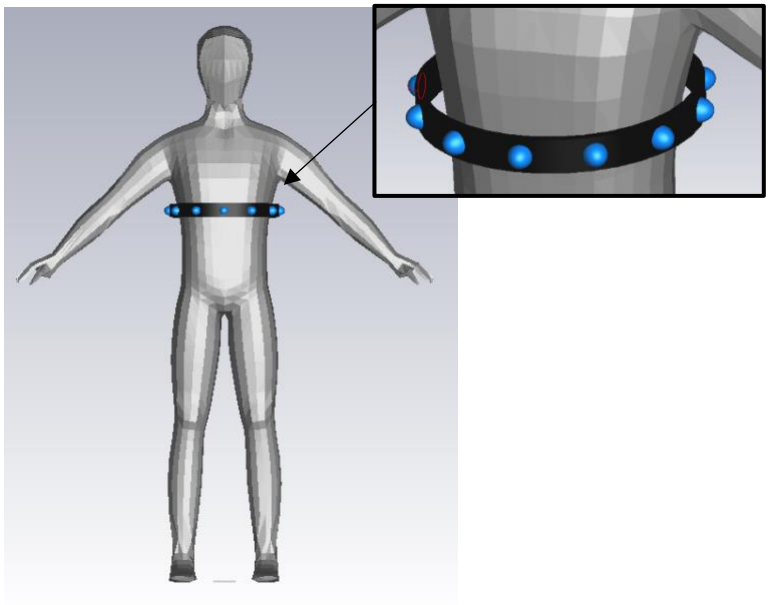

Figure 45: Positioning of the sensors over a radius (representing the assembly in the vest) over the torso of the volunteer carrying the vest of Figure 43.

A similar approach as the one described in the previous section can be carried out to identify the total amount of received power along the ring and identify the related beam overlap and the required number of sensors.

Nevertheless, given the usage of a single ring a choice on the preferred angle of arrival of the RF-EMF field should be made. Given the two use cases which will be considered in Task 7.3, indoor and outdoor environments, with the support of the simulation studies performed in Task 3.2 and Task 3.4 the statistics of the preferred angle of arrival of the signal will be identified.

After this analysis has been concluded, special lens shapes will be synthesized and realized in order to shift the half power beam width to the identified direction in respect to the ring located on the vest.

The synthesis of these lenses will be carried out using the approach developed in [22][23] realizing a final shape as shown in Figure 46.

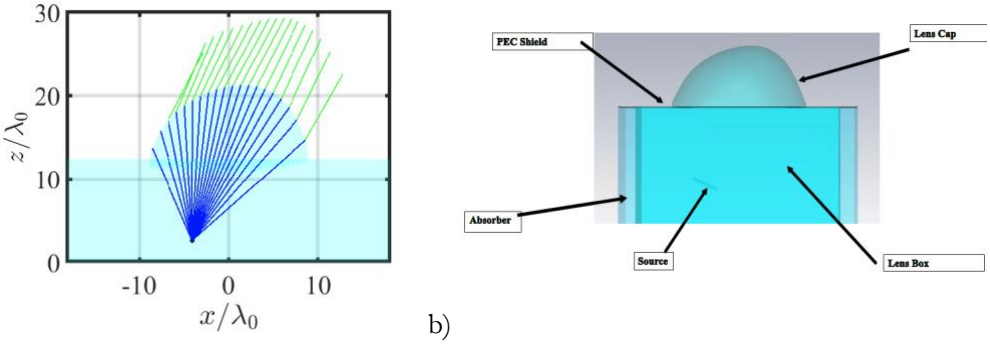

a) b)

Figure 46: a) Ray tracing plot for shaped quartz lens realizing a tilt of 25° in the elevation angle; b) lens antenna geometry exported to the CST environment.

5 NextGEM use case with low-power sensors

The monitoring sensor architectures described in Sections 4.1 and 4.2 will be employed in two use cases which are briefly described here.

5.1 Static sensor deployment at the Green Village

The Do IoT Fieldlab is an open platform located at The Green Village (TGV) [20] in the Delft University of Technology Campus, to test applications based on various communication technologies (including 5G) in a real-life environment.

The area is composed of an urban like environment with street and buildings, as shown in Figure 47 a). The full 3D planimetry, see Figure 47 b), can be used to perform accurate ray tracing simulations as discussed in deliverable D3.2 to identify the coverage and exposure in different scenarios (base station locations, user distribution, use cases, etc.).

a)  b) 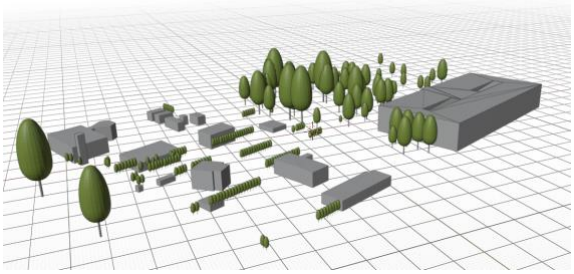

Figure 47: a) Satellite view from google maps of the Green Village at the Delft University of Technology campus, b) 3D planimetry of the Green Village in ArcGIS Pro.

FR1 Testing

The usage of the Green Village as a location to deploy static sensing nodes was tested for the FR1 sensors acquired in a previous project by one of the partners. For this purpose, four nodes shown in Figure 48 a) were deployed in the location highlighted in Figure 48 b).

a)

ɔ)

Figure 48: a) Sensor in case installed in the Green Village, b) location of the sensors (yellow mark) installed in the Green Village.

The TGV infrastructure also includes an online dashboard environment (using Grafana), which was used to record and visualize the measurements acquired by the nodes, see Figure 49, and when the simulation environment will be completed to correlate the measurements with the relative exposure differences.

Figure 49: Dashboard developed in Grafana presenting the output of the sensor installed at the Green Village, showing the diurnal rhythm of the electric field strength at that location.

FR2 Testing

In order to test in the Green Village, the FR2 sensor in realistic "emulative" environments, the request for an experimental license was applied to the Rijksinspectie Digitale Infrastructuur (RDI) agency.

In order to provide the realistic signal environment (i.e., content and scanning capabilities) for the outdoor environment, an 8x8 uniform rectangular phase array was received from NXP and tested in the Ducat anechoic chamber at TU Delft, see Figure 50.

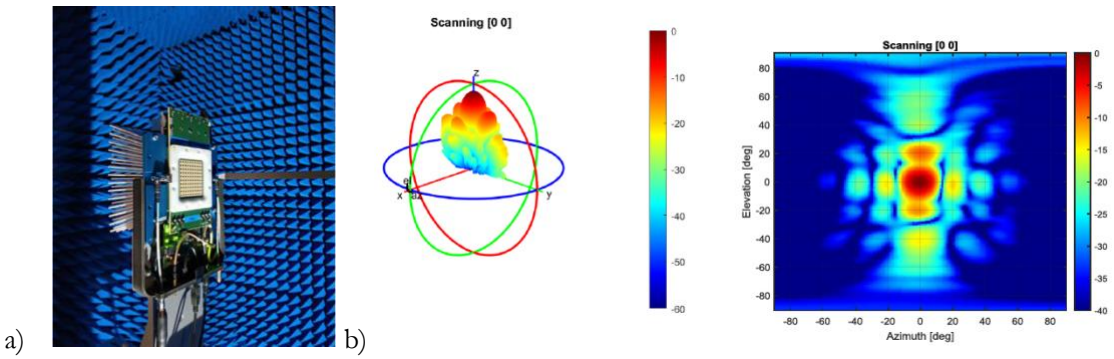

Figure 50: a) NXP 5G FR2 8x8 antenna panel, b) broadside characterization in the Ducat anechoic chamber.

5.2 Static sensor deployment indoor at TU Delft

In order to test the wearable vest in the FR2 band in indoor environments, a 4x4 antenna panel manufactured by Tmytek was selected, as seen in Figure 51 a), and characterized in the Antenna Dome at TU Delft, see Figure 51 b) and c).

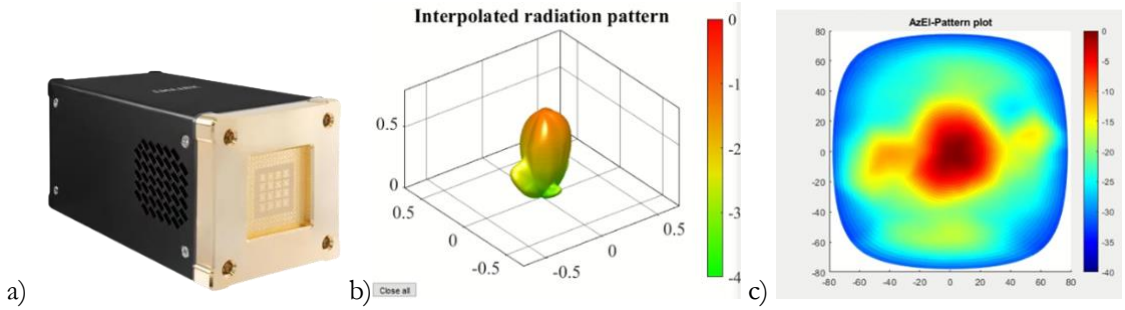

Figure 51: a) TmyTek Bbox FR2, b) measured 3D pattern in the Antenna Dome, c) Azimuth Elevation plane representation.

5.3 Wearable sensor integrated in a vest and helmet

The measuring vest will be deployed in case study 3 for two types of measurements: exposure surveys to assess the exposure in different types of microenvironments, e.g., at home, at work, shopping, elsewhere-inside,

elsewhere-outside, travel [24], and to assess the maximum exposure at the vulnerable positions on the body, i.e. in superficial blood vessels where the electric field within the red blood cells may be maximal.

Of course, the vest can be used in a third kind of survey, the ecological momentary assessment, as an epidemiological survey in which one person is under his own control, i.e. responses in lower and higher exposure situations are compared by following this person for several days and concurrently bodily parameters or self-declared well-being will be registered [25][26].

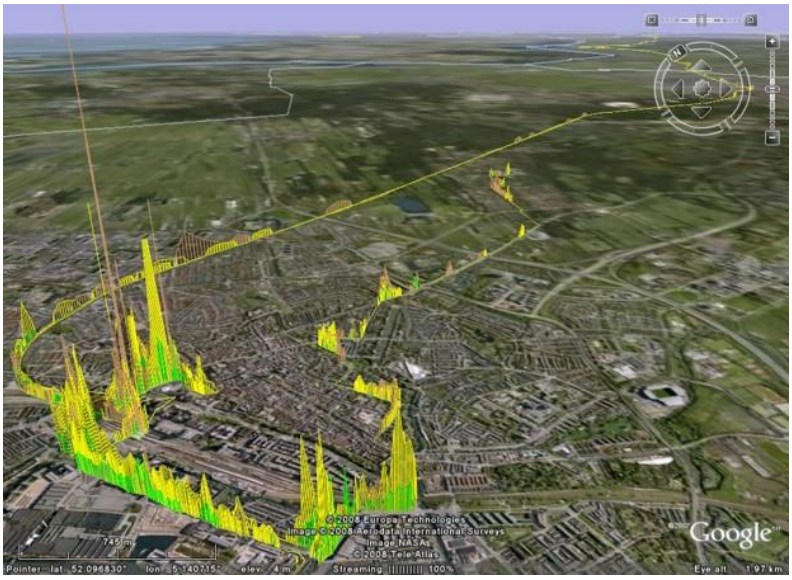

Figure 52: Electric field strength plotted on a map during a bicycle trip and train ride in the city of Utrecht, The Netherlands. The height on the track indicates the electric field strength of the 4G network with stationary beams for mobile phone downlink bands for 900 MHz (brown), 1800 MHz (yellow), 2100 MHz (green).

As the measurement vest adds a GPS location and a timestamp to the measurements, the local exposure for different positions of the body can be shown on a map, displaying the exposure hotspots in time and place. Note, however, that in 5G, the traffic beams are dynamically following the receiver, so these hotspots will constantly change, whilst in 4G systems, antennas transmit in stationary beams directed at locations where the highest demand occurs. Figure 52 shows an example of exposure during a bicycle ride through the city in a 4G mobile phone band.

This principle was also adapted to a helmet: four sensor nodes with mmWave antennas were integrated in a bicycle helmet. Two tests have been conducted: one in the lab and one in-situ in an operational mmWave testbed (COSMOS, https://www.cosmos-lab.org/). During the lab tests, two nodes were found to be not working. During the in-situ test, only one node remained. For the case study measurements, care will be taken to improve the durability of the sensors.

Figure 53: Helm prototype with integrated two (dual polarized) FR2 sensor (prototype zero) realized by the partners and the microcontroller board and logging system developed in the NextGEM and discussed in Section 3.3.1.

Thanks to the improved microprocessor, 5000 samples per second could be taken, measuring (rms) 200 μs per sample, which is equal to 80% or 160% of the slot duration for numerologies μ = 2 or μ = 3, respectively. Of course, this can be adapted.

The 5000 samples were converted from ADC / voltage values to power (in dBm) values, using the approach described in Section 3.3.1. Each of these values was converted to linear received power (in mW) before the average of the samples was calculated. Moreover, the minimum and maximum values were retained. Finally, for each second, the number of values above a power threshold was calculated., from which a duty cycle could be calculated. This measurement is important for estimating the spatiotemporal duty cycle of the network, which acts as a reduction factor in the compliance assessment of advanced antenna systems / massive mimo antennas (IEC 62232).

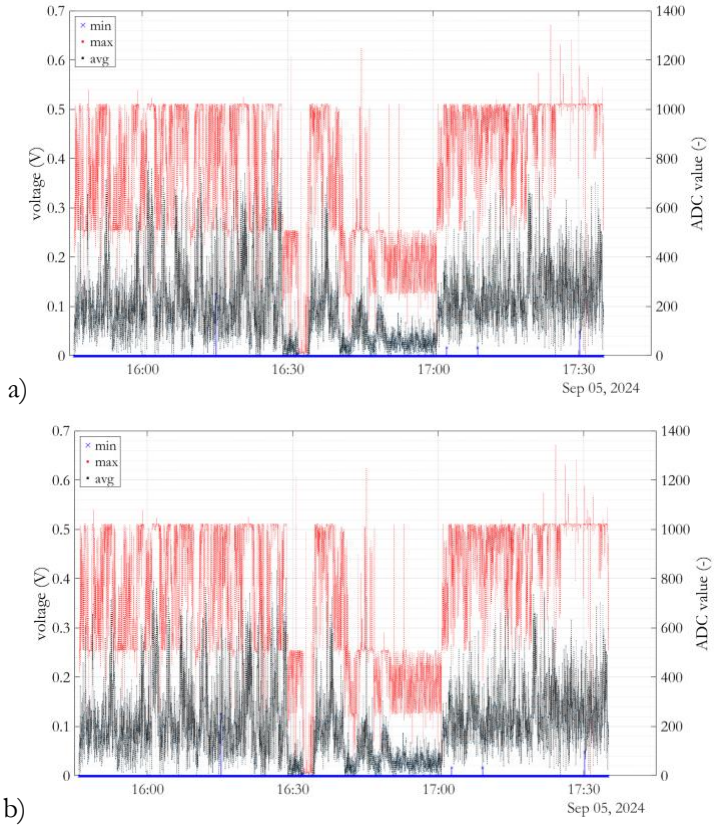

Figure 54: In-situ mmWave measurements with helmet. (a) ADC and voltage (V) levels over time. (b) Duty cycle over time.

6 Conclusion

In this deliverable, we presented a comprehensive review of the technology choices and key performance indicators used in the development of innovative sensors for continuous monitoring of FR2 network activities. The projected performance, supported by detailed simulation analysis and sub-block performance verification, indicates that the developed hardware achieves state-of-the-art results.

We described the key building blocks of the sensor unit from a designer's perspective, highlighting the main trade-off between the observation angle and the device's sensitivity. The selection of commercially available components was justified based on their individual performance and overall impact on the system.

The RF active component's ability to amplify, condition, down-convert, and detect the 5G FR2 signal was tested within a prototype environment to validate the simulation strategy. The antenna design and optimization were conducted using a state-of-the-art design process that combined full electromagnetic strategies with physical optics approaches to account for the response of the plastic lens. This approach was fully validated through experimental results using a prototype of the antenna layer stack and the 3D-printed lens.

Finally, we described the architectures of both the static and wearable sensing nodes, detailing their applications along with the necessary hardware to create the emulative environments for the two case scenarios targeted in WP7.

References

[1] S. Q. Wali, A. Sali, J. K. Allami and A. F. Osman, "RF-EMF Exposure Measurement for 5G Over Mm-Wave Base Station With MIMO Antenna," in IEEE Access, vol. 10, pp. 9048-9058, 2022.
[2] Erdal Korkmaz, Sam Aerts, Richard Coesoij, Chhavi Raj Bhatt, Maarten Velghe, Loek Colussi, Derek Land, Nikolaos Petroulakis, Marco Spirito, John Bolte, "A comprehensive review of 5G NR RF-EMF exposure assessment technologies: fundamentals, advancements, challenges, niches, and implications", Environmental Research, vol. 260, 2024, 119524, ISSN 0013-9351.
[3] ADALM-PLUTO Overview, Available at: https://wiki.analog.com/university/tools/pluto (Accessed: February 16, 2024).
[4] S. Aerts et al., "In-situ Measurement Methodology for the Assessment of 5G NR Massive MIMO Base Station Exposure at Sub-6 GHz Frequencies," in IEEE Access, vol. 7, pp. 184658-184667, 2019.
[5] Frei, P., Mohler, E., Neubauer, G., Theis, G., Bürgi, A., Fröhlich, J., Braun-Fahrländer, C., Bolte, J., Egger, M. and Röösli, M., 2009. Temporal and spatial variability of personal exposure to radio frequency electromagnetic fields. Environmental research, 109(6), pp.779-785.
[6] 100MHz to 40GHz Linear-in-dB RMS Power Detector with 35dB Dynamic Range, Available at: https://www.analog.com/media/en/technical-documentation/data-sheets/5596f.pdf (Accessed: February 16, 2024).
[7] F. A. Musters, R. A. Coesoij, M. D. Migliore, F. Schettino and M. Spirito, "The Antenna Dome Real-Time Distributed Antenna Pattern Characterization System," 2021 97th ARFTG Microwave Measurement Conference (ARFTG), Atlanta, GA, USA, 2021, pp. 1-5.
[8] H. Zhang, S. Bosma, A. Neto and N. Llombart, "A Dual-Polarized 27 dBi Scanning Lens Phased Array Antenna for 5G Point-to-Point Communications," in IEEE Transactions on Antennas and Propagation, vol. 69, no. 9, pp. 5640-5652, Sept. 2021.
[9] Dhaker, Piyu: "Introduction to SPI Interface", Analog Dialogue, Available at: https://www.analog.com/en/resources/analog-dialogue/articles/introduction-to-spi-interface.html (Accessed: February 26, 2024).
[10] QPA2628 Product Datasheet, Available at: http://www.qorvo.com/products/d/da003595 (Accessed: February 16, 2024).
[11] ADRF5731 Datasheet and Product Info, Available at https://www.analog.com/en/products/adrf5731.html
[12] Accessed: February 16, 2024).
[13] A. Ferrero and U. Pisani, "An improved calibration technique for on-wafer large-signal transistor characterization," in IEEE Transactions on Instrumentation and Measurement, vol. 42, no. 2, pp. 360-364, April 1993.
[14] ATMEGA328PB documentation page, Available at: https://www.microchip.com/en-us/product/atmega328pb (Accessed: February 18, 2024).
[15] LTC2312-12 documentation page, Available at: https://www.analog.com/en/products/ltc2312-12.html (Accessed: February 18, 2024).
[16] AVR-GCC Wiki page, Available at: https://gcc.gnu.org/wiki/avr-gcc (Accessed: February 18, 2024).
[17] M. Alonso-delPino, M. d. Rosa, M. Simeoni, M. Spella, C. De Martino and M. Spirito, "A Planar Near-Field Setup for Millimeter-Wave System-Embedded Antenna Testing," in IEEE Antennas and Wireless Propagation Letters, vol. 16, pp. 83-86, 2017.
[18] C.A. Balanis, Antenna Theory: analysis and design, 3rd edition, John Wiley & Son, ch. 17, pp 1014-1021, 2005.
[19] R. A. Coesoij, F. A. Musters, D. Roos, T. van Velden and M. Spirito, "Calibration approaches in Multi-Node Antenna Characterization Setups," 2023 100th ARFTG Microwave Measurement Conference (ARFTG), Las Vegas, NV, USA, 2023, pp. 1-4.
[20] The Green Village documentation page, Available at:https://www.thegreenvillage.org/ (Accessed: February 26, 2024).
[21] S. Aerts, G. Vermeeren, M. Van den Bossche, R. Aminzadeh, L. Verloock, A. Thielens, P. Leroux, J. Bergs, Braem, A. Philippron, and L. Martens, "Lessons learned from a distributed RF-EMF sensor network," in Sensors 22, no. 5, 2022.
[22] H. Zhang, S. O. Dabironezare, J. J. A. Baselmans and N. Llombart, "Focal Plane Array of Shaped Quartz Lenses for Wide Field-of-View Submillimeter Imaging Systems," in IEEE Transactions on Antennas and Propagation, vol. 72, no. 2, pp. 1263-1274, Feb. 2024.
[23] L. Gottmer, "A GO/PO tool for synthesizing shaped multi-surface dielectric lens antennas", Master Thesis, Delft University of Technology, 2022.

[24] Bolte JF, Eikelboom T. Personal radiofrequency electromagnetic field measurements in The Netherlands: exposure level and variability for everyday activities, times of day and types of area. Environ Int. 2012 Nov 1;48:133-42. Doi: 10.1016/j.envint.2012.07.006.

[25] Bogers R.P., Van Gils A., Clahsen S.C.S., Vercruijsse W., Van Kamp I., Baliatsas C., Rosmalen J.G.M., Bolte J.F.B., 2018. Individual variation in temporal relationships between exposure to radiofrequency electromagnetic fields and non-specific physical symptoms: A new approach in studying 'electrosensitivity'. Env. Internat. 121: 297–307.

[26] Bolte JFB, Clahsen S, Vercruijsse W, Houtveen JH, Schipper MA, Van Kamp I, Bogers R., 2019. Ecological momentary assessment study of exposure to radiofrequency electromagnetic fields and non-specific physical symptoms with self-declared electrosensitives. Environ. Int. 131 – 141.